Scanning electron and optical microscopic studies of the system of porcine zonular fibres

Zoltán Imre Bocskai[1], Zoltán Kiss[2], Gábor László Sándor[3], Imre Bojtár[1], Zoltán Zsolt Nagy[4]

[1]Budapest University of Technology and Economics, Faculty of Civil Engineering, Department of Structural Mechanics

[2]Budapest University of Technology and Economics, Faculty of Mechanical Engineering, Department of Polymer Engineering

[3]Semmelweis University, Department of Ophthalmology

[4]Semmelweis University, Department of Ophthalmology and Faculty of Health Sciences

zbocskai@mail.bme.hu

Abstract

The mechanical behaviour of the zonular apparatus greatly affects the accommodation process because it moves out from the ciliary muscle and runs into the lens capsule. The zonular fibres convey the force between the ciliary body and the crystalline lens. For the measurement of the mechanical properties of zonular fibres is necessary to know its geometry. In this paper we analyzed the network of porcine zonular fibres with scanning electron and optical microscope. We manifested that the porcine zonular fibre system differs from human and monkey eyes. The thickness of the apparatus of intertwined zonular fibres is approximately 45 μm and the length from the origin to the insertion is about 1.5 mm. Based on these informations the input parameters of numerical modelling can be more precise to clarify the accommodation process.

Keywords: zonular fibres, bundles, scanning electron microscope

1. Introduction

The zonular fibres play a major role in the mechanism of accommodation. The force from the ciliary body is transferring to the lens through the zonular fibre system.[1] Based on the Helmholtz theory[1] the geometry of the apparatus of the zonules is very important at the accommodation process of the eye. For measuring of the mechanical properties of these fibres – for example with tension tests – we need the geometry e.g. thickness and length parameters of the bundles. Many papers have been dealt with the analysis of zonules usually with electron microscope.[2–6] For the investigation of the mechanical behaviour of zonular fibres in macroscopic level first of all we need the geometry of the network system. There are only very few data about the size of the zonular bundles.[7] Our purpose in this paper is to investigate the bounding dimension of the zonular group with three different methods. We used scanning electron microscope for the first method and optical microscope for the second and the third one. The network of the fibre system was not considered in details.

2. Materials and Methods

The porcine eye samples were harvested from a local slaughterhouse. We obtained the globes of the eyes (bulbus oculi) from 6–7 months old, weighing 100–120 kg, male animals. The transport time from the slaughterhouse to the laboratory was one and the half hours. The transport temperature was +4 degree of Celsius and

it was held with cooler bag. 20 eyeballs were included in this study. 5 eyeballs were used for the scanning electron microscope analysis and 10 (5-5) for the optical microscope analysis. The remaining globes with obvious deformation or damage were excluded. The network and the thickness of the zonular group were analyzed in three different ways. In every case we took care about the integrity of the zonular network, when we removed – with scissors and forceps – the posterior side with the aqueous humour and the hyaloid membrane. After this step the cornea has been removed at the limbus and finally the iris. Samples were prepared and analyzed as quickly as possible to avoid any biological decomposition.

2.1. Measuring with scanning electron microscope (SEM)

The specimens were fixed for scanning electron microscopy in 8% paraformaldehyde. The fixed samples were dehydrated in a series of ethanol dilutions (20%-96% vol/vol), fol-

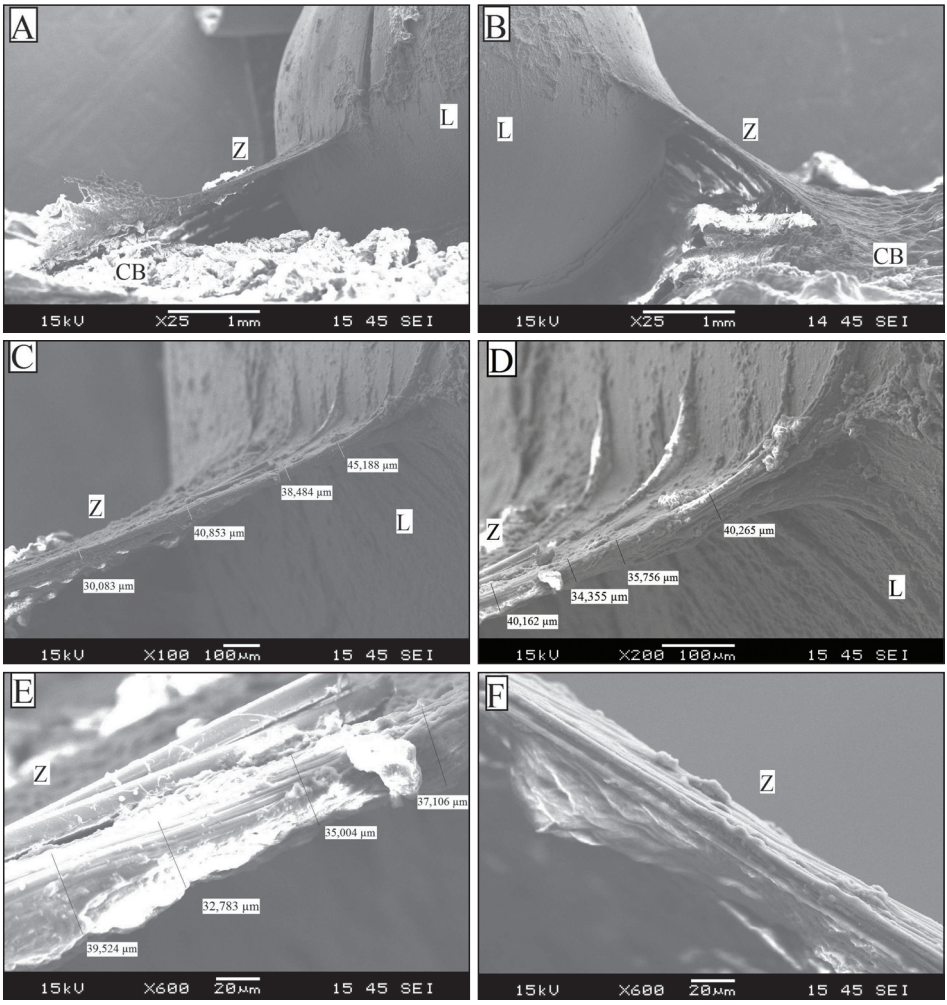

Figure 1. SEM images about the zonular bundles L: lens; Z: zonules; CB: ciliary body

lowed by vacuum-drying. The specimens were mounted on double-sided carbon tape, sputter coated with gold and images were taken at various magnifications with scanning electron microscope JSM 6380LA (JEOL Ltd., Tokyo, Japan) and with the manufacturer's software. *Figure 1* shows some of the SEM images.

2.2. Measuring with optical microscope (OM I. and OM II.)

We would like to measure the average thickness dimension of the zonular group as we stated in the introduction part thus we analyzed the samples with optical microscope also (Olympus BX 51M, Olympus Corporation, Tokyo, Japan) with two different methods.

In the first way the eyeballs were slightly fixed in 8% formaldehyde solution for 24 hours. After this step the zonular fibres with the crystalline lens in the slightly fixed position were prepared because in the eyeball the intraocular pressure causes certain amount of tensile strength in the fibres despite the fact that after the death the state of rigor mortis occurred during 2-4 hours. In this position we made a section toward the zonules, the lens and the ciliary body. With this method we got a sample what could help to analyse the thickness of the zonular apparatus with optical microscope (OM I.). *Figure 2* shows some of the images and the measured thickness values.

In the second way of optical microscope examination (OM II.) we cut the posterior part behind the lens (sclera, choroid, retina and vitreous body) and the anterior side with the cornea and iris from the fresh eyeballs. The hyaloid membrane was removed very carefully. Thus we have the intact (2 hours delayed from the slaughtering) anterior side with the lens, zonules and ciliary body with the narrow stripe of sclera without any fixative to preserve a native in situ architecture. These prepared specimens were filled with polyester resin. We waited until the resin become solid and then made a section across the lens, zonules and ciliary muscle. After these steps the specimens were polished with Struers (Struers GmbH, Germany) automatic polishing machine then we could analyse the surface of the section with the optical microscope. With this method the thickness of the group of intact zonular fibres was measurable – without any dehydration – according to the gap between the solid layers of resins (green and black layers in *Figure 3*). Some of the images and the measured thickness values are in *Figure 3*.

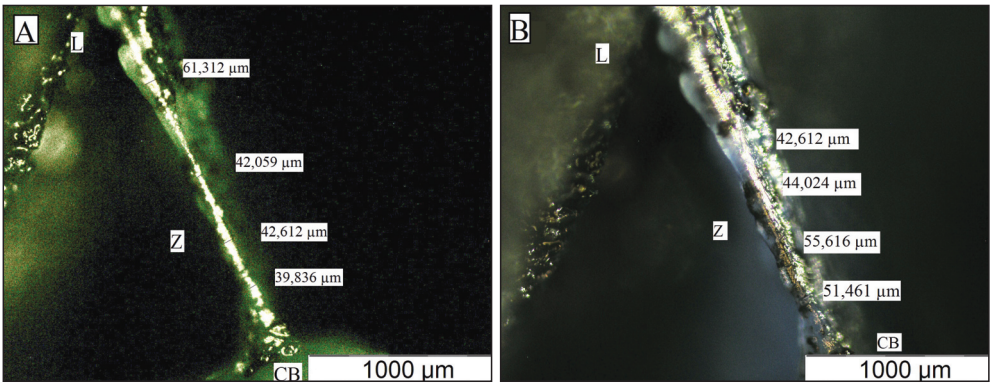

Figure 2. Optical microscope images about the zonular bundles L: lens; Z: zonules; CB: ciliary body

3. Results

The thin filaments run up to the equatorial edge from the interlacing zonular bundles (*Figures 1/D and 4/A)*. In *Figure 1/A–B* and in *Figure 4/B* we can see that the zonular filaments attached to the bottom of the basis of ciliary body valleys. Near the equatorial connections the zonular bundles become more organised and approximately parallel as you can see in *Figure 1/E–F* until the origin from the ciliary valleys. This roughly parallel structure of the

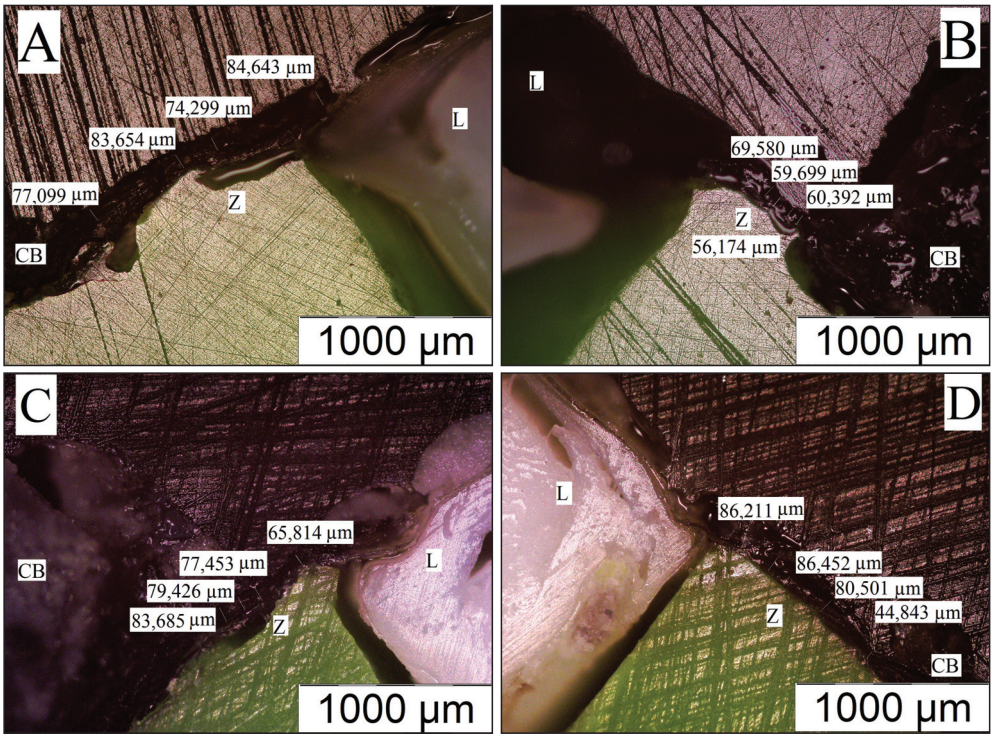

Figure 3. Optical microscope images about the zonular fibres in the resin cast L: lens; Z: zonules; CB: ciliary body; black: anterior side; green: posterior side

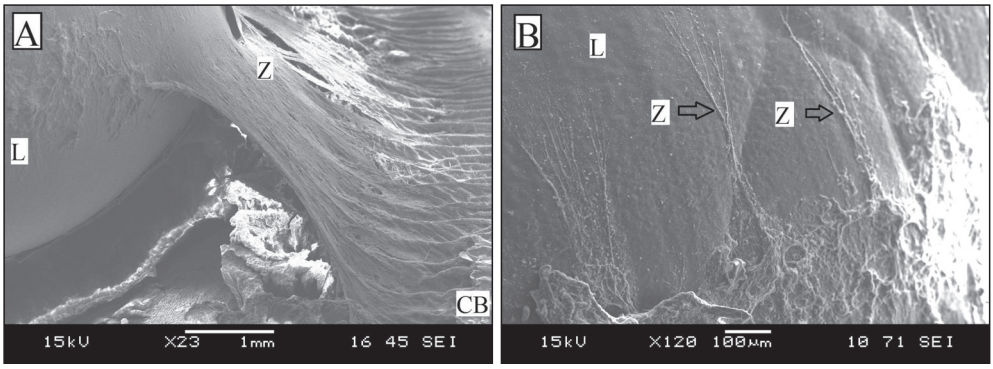

Figure 4. SEM images about the origin and insertion of the zonular bundles L: lens, Z: zonules

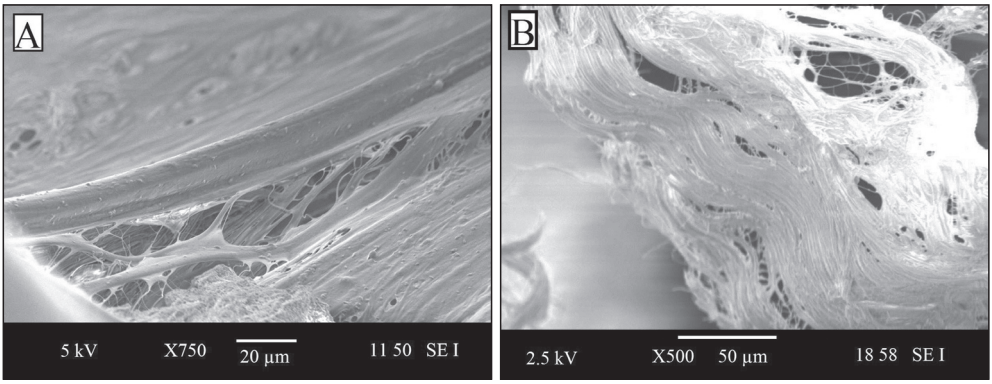

Figure 5. SEM images about the filaments and their interlacing

zonular network is permanent between the start and the end areas *(Figure 1/A–C)*. The interlocking collateral layout is more conspicuous in higher magnification as shown in *Figure 5*.

Figure 6 shows the evidence of the tension force – despite of the rigor mortis – in the zonular fibres. According to the fact that during the preparation for SEM measurements at few samples the zonules injured or torn due to dehydration. As you can see in *Figure 6* the filaments after the disruption became curled because fundamentally tensile force loaded them.

The thickness of the zonular apparatus of each specimen was measured in four different positions where the bundles were close to constant size and parallel as we mentioned before.

We measured the lowest average thickness value with scanning electron microscope: 33.2 ± ±9.1 µm. With the second method (OM I.) the average thickness was a bit wider: 43.2 ± 9.6 µm. The third method (OM II.) resulted in an average 73.1 ± 12.5 µm thickness for the bundles. *Figure 7* shows the mean thickness values and the standard deviations and the minimum/maximum values based on the three different methods.

We also measured the length of the bundles from the ciliary muscle to the lens capsule. According to the SEM images we have an average 2.18 ± 0.25 mm length for the bundles. The optical microscope analyses showed 1.92 ± ±0.05 mm and 1.18 ± 0.37 mm average length value (OM I. and OM II.). *Figure 7* also shows

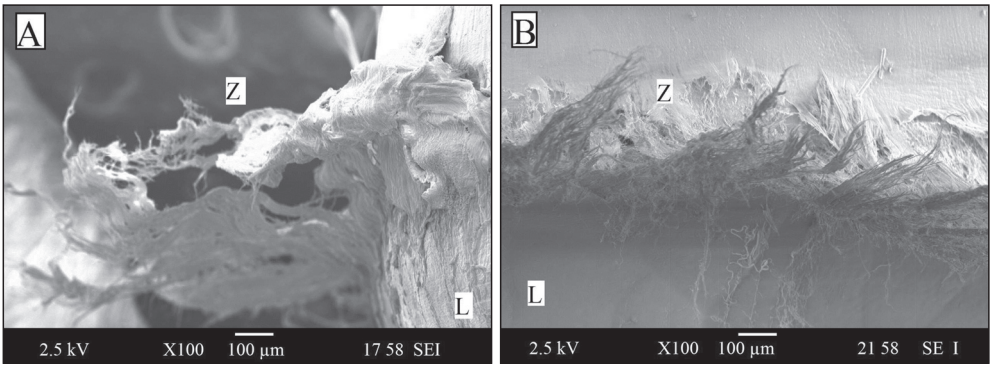

Figure 6. SEM images about the torn fibres, side view and front view L: lens; Z: zonules

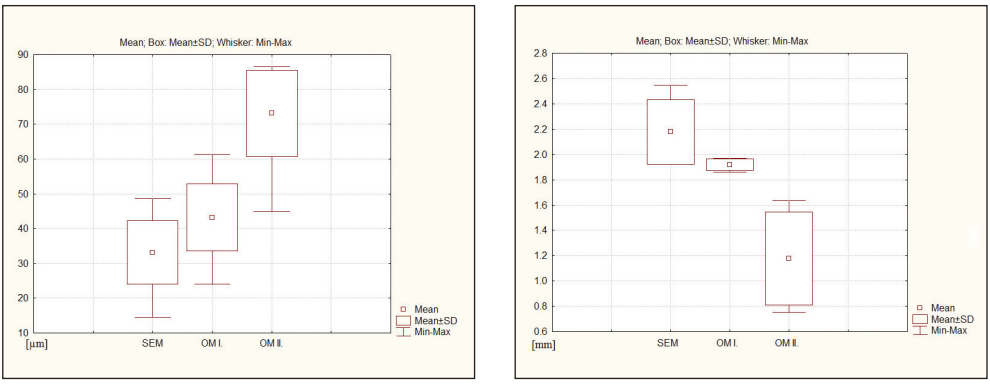

Figure 7. Results about the thickness and the length of the bundles (SEM, OM I., OM II.)

the results about the length of the zonular bundles from the three different methods in a statistical way.

4. Discussion

We can state that – based on the scanning electron microscope images – the network of the zonular fibres differs from the human and monkey zonules.[2,5] As shown in *Figure 1* it is obvious that the zonular network only connected at the equatorial stripe of the lens. We can see in *Figure 1/D* that the zonular fibres spread at the equatorial line of the lens but their structure is clearly distinguishable from the lens capsule.

We also concluded the average thickness of the porcine zonular bundles with different methods. The thickness was noticeably larger with OM II. method than with SEM or OM I. methods. This result was expected because the samples for SEM were almost completely dehydrated and the specimens for OM II. had natural moister content. The OM I. method resulted in the thickness values between the two other methods because in this case the moisture content was also between the other two hence these results served a control measurement.

All of the used methods have advantages and disadvantages (e.g. hydrated and dehydrated conditions, fixed and non-fixed states) but according to our opinion these techniques are reliable to estimate the minimum and the maximum range of the thickness of the bundles.

The average thickness values are comparable with reference[7] who measured the thickness values of bovine zonular apparatus. They have been reported 45–55 μm thickness but it should be noted that they used digestive enzyme (hyaluronidase) during their preparation technique.

The length measured by OM II. method was a bit shorter than the length with the other two methods because at SEM and OM I. analysis the ciliary muscle of the samples was in slightly different position. We saw longer length at SEM and OM I. because the crests of the ciliary process were in lower position thus the whole length of the zonular fibres was visible according to their origin from the bottom of the ciliary valleys.

Based on our analyses we can state that the geometry of the zonular bundles is given thus we can measure the mechanical parameters in easier way and we can refine the theory of the dynamic accommodation mechanism.

References

1. *Bocskai Z, Bojtár I.* Biomechanical modelling of the accommodation problem of human eye. Periodica Polytechnica Civil Engineering 2013; 57(1):1-7.

2. *Bernal A, Parel JM, Manns F.* Evidence for posterior zonular fiber attachment on the anterior hyaloid membrane. Investigative Ophthalmology & Visual Science 2006;47:4708-13.

3. *Curtis R.* The suspensory apparatus of the canine lens. Journal of Anatomy 1983;136:69-83.

4. *Farnsworth PN, Mauriello JA, Burke-Gadomski P, Kulyk T, Cinotti AA.* Surface ultrastructure of the human lens capsule and zonular attachments. Investigative Ophthalmology 1976;15:36-40.

5. *Rohen JW.* Scanning electron microscopic studies of the zonular apparatus in human and monkey eyes. Investigative Ophthalmology & Visual Science 1979;18:133-44.

6. *Streeten BW.* The zonular insertion: a scanning electron microscopic study. Investigative Ophthalmology & Visual Science 1977;16:364-75.

7. *Wright DM, Duance VC, Wess TJ, Kielty CM, Purslow PP.* The supramolecular organisation of fibrillin-rich microfibrils determines the mechanical properties of bovine zonular filaments. The Journal of Experimental Biology 1999;202: 3011-20.

The work reported in the paper has been developed in the framework of the project „Talent care and cultivation in the scientific workshops of BME" project. This project is supported by the grant TÁMOP-4.2.2.B-10/1–2010-0009.

Zoltán Imre Bocskai
Budapest University of Technology and Economics, Faculty of Civil Engineering
H–1111 Budapest, Műegyetem rkp. 3. K ép. mf 63.
Tel.: (+36) 1 463-1434

Compression test of the mandibular cortical bone: A cadaver study assessing formalin treated or macerated bone specimens

János Simonovics[1], Péter Bujtár[2], Károly Váradi[1], Attila Szűcs[3], Zsolt Fejér[4]
[1]Budapest University of Technology and Economics, Department of Machine and Product Design
[2]University Hospitals of Oulu, Department of Oral and Maxillofacial Surgery
[3]Semmelweis University, Department of Oro-Maxillofacial Surgery and Stomatology
[4]Semmelweis University, Department of Human Morphology and Developmental Biology
janos@simonovics.hu

Abstract
Nowadays the examination of implants from engineering point of view is becoming more and more supported in the medical field. Instead of the more problematic cadaver examination, the computer based simulations are growing more popular. The examinations must be validated to be able to stay with the realistic situation.
Using these engineering methods it became possible to do measurements on the reconstructions of a human resectioned mandible. The creation of the bone models is one of the most varying fields in the biomechanical simulation. In the literature a wide range of Young modulus for the bone cortical layers can be found and these values are actively used even in different further finite element simulation researches. However the proper modeling of the cortical layer thickness and correctly calibrated mechanical parameter settings bare key importance regarding the stability and connection of the implants and the fixing screws.
The values of the Young modulus are depending on many factors, for example gender or even the age, not even mentioning further different influencing factors.
In this study destructive biomechanical examinations were carried out on bones received from dead people. The samplings of the bone were conducted from the area of the screwing used in the mandible reconstruction. Considering the results it can be concluded that the values in the literature are often not as accurate. Regarding orthotropic values of the mandible, so far has only been a small segment of information was covered.
The measured values are lower than the ones in the literature. In case of the highest value it is still 3.5 GPa Young modulus in the axial direction. The results can be used in order to create a more reliable model combined with a more realistic Young modulus for the finite element simulation of the bone models. On these models the different scenarios of the resection cases can be estimated more precisely with examinations.

Keywords: mandible, compression, Young modulus, bone

Introduction

In case of cancer, the more important factor is prevention. Narrowing it to the oral cavity cancers, most of them can be discovered with physical examination hence can be screened easily. The earlier the realization, the more lives can be saved. In Hungary every year approximately 1700 people die out of the 3000 discovered cases in the field of oral cavity can-

cer. In light of these numbers we are on top of the list within Europe. In both female and male cases Hungary takes the number one spot considering the death toll from oral cavity cancers.[1] Despite the easy detection of the problem most of the patients are too late, in which case a radical intervention cannot be avoided to save their lives, this way also reducing the chances of full recovery. The treatment of oral cavity cancers always depend on the location where it developed within the mouth, what is the extent of the development and how is the condition of the patient. When the jaw (mandible) is affected, the chances are very high that a surgical intervention is needed, during which the affected bone section will be cut out (resection).

During the resection the surgeon removes the bone allocation affected by the cancer. The resection can be partial or full depending on the extent of the bone. The effect on the mandible can be partial or full loss of function, further more often the mechanical load carrying role weakens or completely disappears.

The resection is unique in every case. It depends on the patient and the situation; therefore we cannot really distinguish between different scenarios from the surgeon point of view. However in most of the cases it can be divided into zones *(Figure 1)*.

In the clinical practice there are two methods existing, which are highly dependent on the extent of the resection, furthermore on the structural quality of the remaining bones in the vicinity of the environment of the resection. One of these is the bone graft method. This can be used in case the bones are in good condition around the area of the resection. The fixation of the graft is realized with a plating technology.

In case of bones in worse condition or the extent of the resection is too big, only the plating technology can be used. There is a great variety of these plates exist. The thickness and length of these plates are selected by the surgeon based on the clinical case and needs of the patient. The length of the plate is selected considering the proper fixation with screws based on the extent of the resection. The plates are deformed based on the geometry of the bone in each case, therefore providing a unique shape for each patient. Each side of the resection usually 3-4 screws are used to fix the plates.

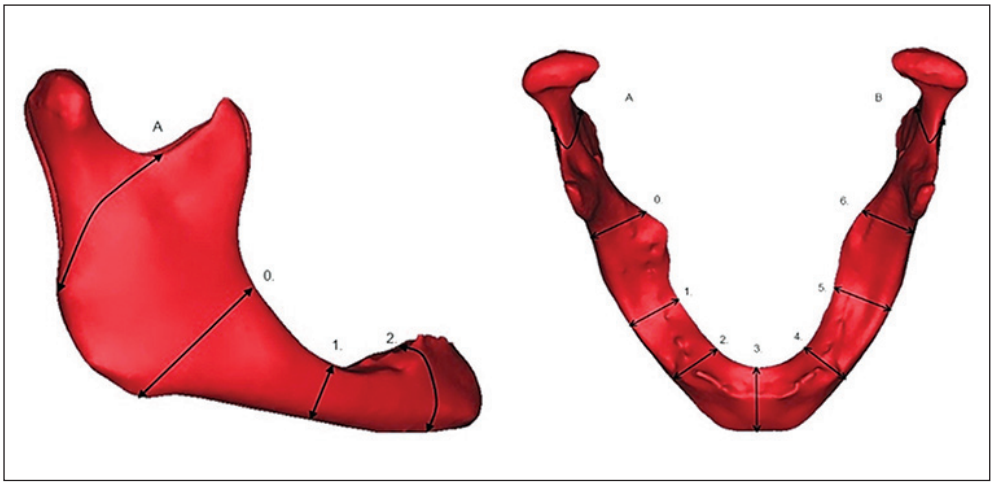

Figure 1. Important resection areas

The screws can be divided into categories; monocortical and bicortical depending on the location and the size of the mandible section. The bicortical screw of course goes through the bone in such a depth that the connection in the counter cortical (hard) layer is big enough. In some cases it completely goes through, therefore the length of these screws is varying. Further we can distinguish among the new methods the so called Locking and Non-Locking systems. In case of the Locking system the screw head and the screw in the plate as well is created with sunken (low) threads, hence providing the secure fixation. However in the Non-Locking system only the plate holes are created with sunken (drawn) method therefore providing the appropriate connection.

The implants used in oral surgery are most of the cases made of an alloy of titanium (TiCP – titanium commercial pure, Ti6A17Nb, etc.). The value of Young modulus is between 90–100 GPa and the 0.3 Poisson coefficient.

Methods

The environment of the fixing screws for the implants is highly important considering the bones. The finite element simulations are becoming more and more popular in the biomechanical field compared to the often problematic cadaver examinations. In the models used for the simulations and also present in the literature are rarely or not at all considered the thickness of cortical allocation and the real mechanical properties. However these properties of the bone allocations can be shifted in a wide range and one by one can be very different. Examinations carried out with these models do not provide a realistic picture of the situation regarding the real relationship between the plates and screws.

For the examination the samples were selected from the area affected by the implant screws during the reconstruction. The samples were taken out of dead human formalin fixed and macerated mandibles. These samples were examined using a mechanical destructive method.

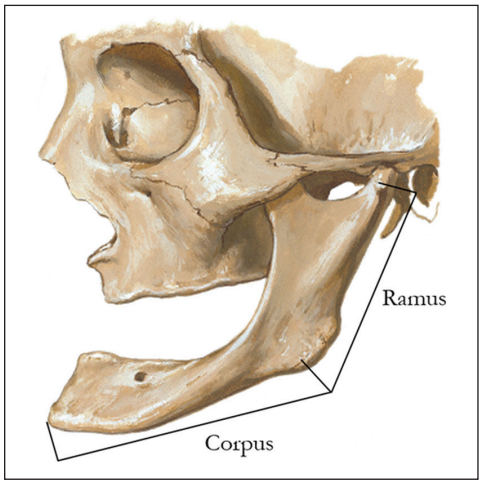

Figure 2. Toothless mandible of aged person

These screw locations in the clinical practice were also affected the corpus and ramus *(Figure 2)*.

The purpose of the formalin fixation is to stop the decay of the enzymes. The water based formaldehyde is one of the most popular fixation methods. During the fixation the fixing solution/material penetrates the deeper regions of the tissues; therefore during the process the damage of the tissue structure is almost unavoidable. During the preparation using the macerated method while applying the warm water the soft regions are decomposed, the bone is steamed and whitened. The osteocollagen systems and salt of the bone stays intact during the preparation, therefore the mechanical properties do not change significantly.[2]

The sampling took place at the Semmelweis University of Human Morphology and Development Biology Department. The use of bone samples were approved by Committee of Sci-

Figure 3. Sampling from macerated mandible

Figure 4. Sampling from formalin fixed mandible

entific and Research Ethics. The heads kept in formalin from which the samples were taken are stored more than 2 years in formalin. The damage of the tissues was so high in some areas, where during the sanding process the samples basically dissolved by the high amount of load.

For the samples 6 mm inner diameter and 10 mm height bone segment was used, which was constantly cooled during the process. All together 96 helical samples was created from 3 formalin fixated and 6 macerated toothless aged human (male and female) mandibles *(Figures 3–4)*.

The mandible is considered to be a complex bone because of its shape. The orthotropic structure is constantly changes with the geometry.[3]

The mechanical parameters from the cheek side and also from the oral cavity side can be entirely different, therefore when creating the samples the different orientations of the bones were marked. After the samples were created the spongiosa allocations were removed, than a special sending process was applied. As a result the samples took the shape of a square geometry with 4 mm × 4 mm cortical thickness. After the structural storage in order to carry out the finite element simulations CBCT/CT scanning was performed on the samples with the help of a unique validation scheme. After the scanning randomly (disregard of sample location and order) compression examinations (pressing machine) were carried out at the Budapest University of Technology and Economics in the Cooperation Research Center for Biomechanics. During the examination the samples were divided into 3 sections and the orthotropic properties were observed focusing on the more precise determination of the Young modulus. Axial, radial and tangential orientations were examined based on the original position of the bone. As the expectation of the highest elasticity modulus was in the axial orientation, therefore the number of sampling was increased regarding the important macerated samples. As a result of the sanding process, many samples were rendered useless in the measurement aspect.

There were 80 from formalin fixed and macerated mandible samples which could be measured correctly, already excluding the ones that could not be worked with. The mixture of measurement orientations were the following *(Table 1)*:

Measured samples that can be evaluated	Axial	Radial	Tangential	Sum
Formalin fixed mandible samples	12	9	11	32
Macerated samples	26	10	12	48

Table 1. Examined samples

Before the compression examination the geometrical measurement of each sample was done and documented. Force-displacement curve graphs were created from the results in light of the Young modulus consideration. The measurements were conducted within normal circumstances. The examination was carried out with a 25 kN limited force measuring cell on an Instron 8872 machine *(Figures 5–6)*. The load velocity was defined to be 0.5, the measurements were conducted until the actual sample destruction based on the force-displacement curve.

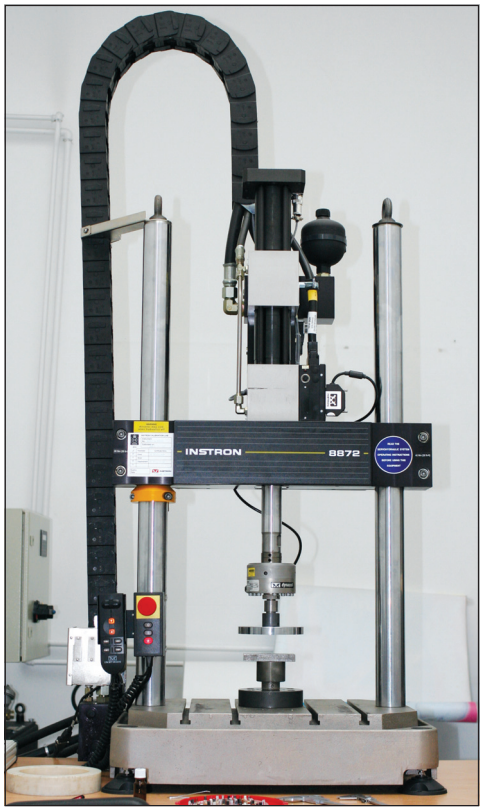

Figure 5. Compression test and a measured sample

The samples inside proper storage containers were sent back to the Semmelweis University Human Morphology and Development Biology Department, where they were finally destroyed.

Results

During the compression examination the force-displacement variables of the bone were registered *(Figure 7)*. The data from the linear sections of the curve and the previously documented size parameters from the bone samples were used for the determination of the Young modulus.

The compression examinations on the bones found in the literature bear a high spread regarding the result data. This can be connected with the unique properties (gender, age and other factors) as well as the storage

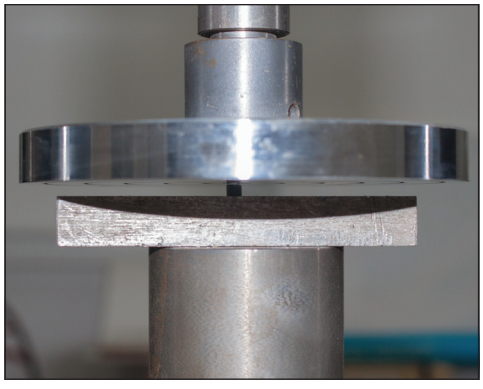

Figure 6. A measured bone sample

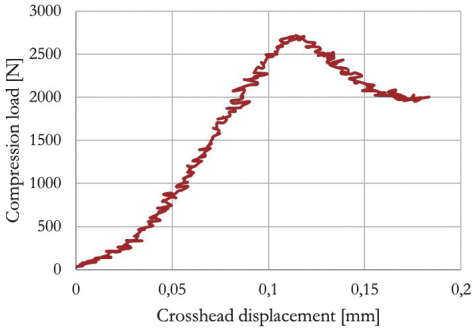

Figure 7. Load-displacement diagram of the 9th macerated bone sample – axial compression

of the bones.[4] There is not much information available for the mandible mainly focusing on the orthotropic properties within the cortical allocations during the compression examination. Isotropic data can be found between 1.5–15 GPa.[5] These values are below the average which can be found in the literature. In the technical literature refers to the average value of 14–23 GPa Young modulus, which is actively used for simulation purposes.[6] On the other hand it is an overstatement to even use this for a mechanical simulation for example in a case of an aging human.

The current study shows that the values from the compression examination are below compared to the literature in both the formalin fixed and macerated bone cases. Hence the consideration of these values can be crucially important in order to create a more realistic model for example in case of a mandible reconstruction of an elderly human. Furthermore it is important from the mechanical point of view to divide properly the bone allocations and to define the material properties.[7]

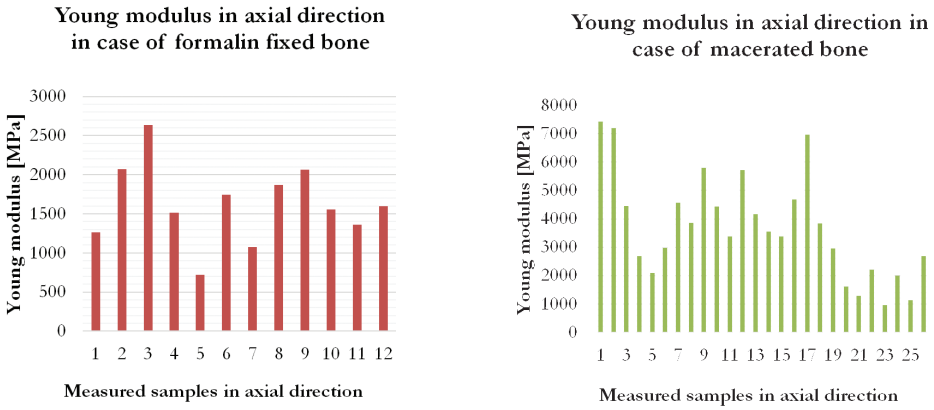

Figure 8. Young modulus in axial direction

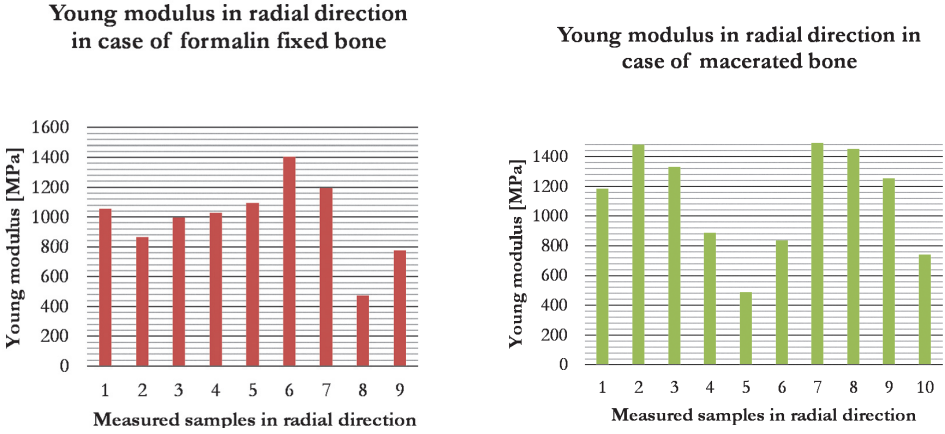

Figure 9. Young modulus in radial direction

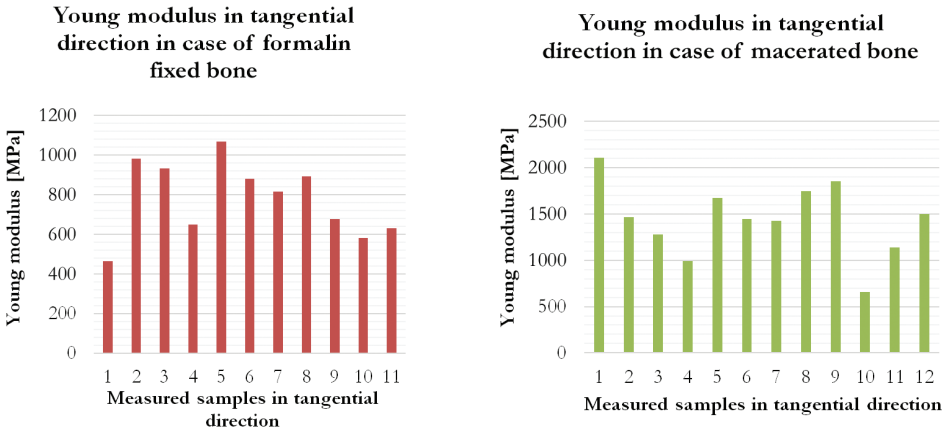

Figure 10. Young modulus in tangential direction

The measured values can be seen on the next diagram and for the sake of better understanding the different orientations and bone types were shown separately *(Figures 8–10)*.

The difference between the Young modulus, the average values and the spread in the values of different orientations shown in a box-plot diagram can be seen quite well in both cases of the formalin fixed and macerated samples *(Figure 11)*. On the diagram considering the 50% median, the lower and upper percentile of 25 and 75% was defined (quartile). This way making more strict the generally used normal domains of 2.5–97.5% and the 5–95%. It is transparent that the mechanical properties of the formalin fixed mandible samples were changed during the fixing. Substantial tissue damage could have occurred in case of the samples due to the storage for possibly more than 2 years. The axial orientation produced more favorable values in both sample cases

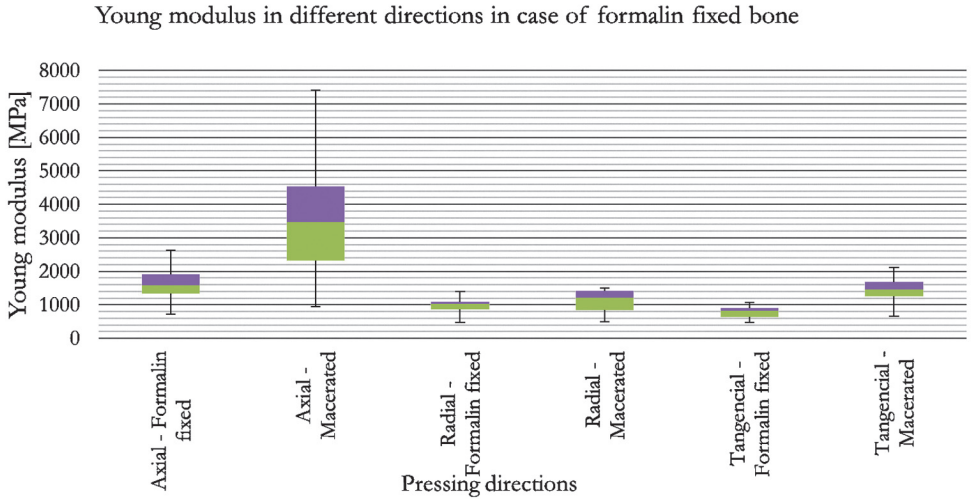

Figure 11. Young modulus in different directions in case of formalin fixed bone

than the radial and tangential orientation, conforming to the different bone types found in the literature.[8,9] The tangential orientation in some measurements of the macerated samples showed better properties than the radial orientation, focusing on the Young modulus. In case of the formalin fixed samples the situation is reversed. The radial orientation compression examination shows better values in the Young modulus.

Summary

Medical treatment of jaw cancer becomes more and more important as the number of diagnosed patients has risen significantly. It is inevitable to understand the correct properties of the mandible in order to provide an adequate reconstruction. Cadaver examinations are available to determine the mechanical parameters.

During this study a compression examination was carried out in orthotropic orientations on toothless mandibles from dead humans both on formalin fixed and macerated samples. The determined Young modulus values registered after the examinations are greatly differing from the values that can be found in the general literature. The results from the samples with significantly different mechanical properties could have key importance in further biomechanical examinations. In the field of model creation the results show that the uniquely changing mechanical properties cannot be excluded in order to create a more realistic model. The collected results can be well used in the finite element analysis method that is becoming more and more popular. These examinations can provide better estimations in the other areas of oral surgery regarding the possible loads. Considering the possibility of improvement, the probability of more stability and faster recovery can be provided for the patients.

REFERENCES

1. *Levi F, Lucchini F, Negri E, Boyle P, La Vecchia C.* Cancer mortality in Europe, 1995–1999, and an overview of trends since 1960. Int J Cancer 2004 Jun 10;110(2):155–69.

2. *Szentágothai J, Réthelyi M.* Funkcionális anatómia. Budapest: Medicina Könyvkiadó Rt.; 2002.

3. *Nomura T, Gold E, Powers MP, Shingaki S, Katz JL.* Micromechanics/structure elationships in the human mandible. Dent Mater 2003;19(3):167–73.

4. *Thomsen JS, Niklassen AS, Ebbesen EN, Brüel A.* Age-related changes of vertical and horizontal lumbar vertebral trabecular 3D bone microstructure is different in women and men. Bone 2013 Nov;57(1):47–55.

5. *Nakajima K, Kondoh J, Fujiwara M.* An experimental study on the dynamic traits of dehydrated mandibles in relation to Yang's modulus and Poisson's ratio of compact bone. Shika Gakuho Dent Sci Rep 1984 Dec;84(12):1951–61.

6. *Kimura A, Nagasao T, Kaneko T, Tamaki T, Miyamoto J, Nakajima T.* Adaquate fixation of plates for stability during mandibular reconstruction. J Cranio-Maxillofac Surg 2006 Jun;34(4):193–200.

7. *Simonovics J, Bujtár P, Váradi K.* Effect of preloading on lower jaw implant. Biomechanica Hungarica 2013;6(1)21-28.

8. *Lawrence Katz J, Yoon HS, Lipson S, Maharidge R, Meunier A, Christel P.* The effects of remodeling on the elastic properties of bone. Calcif Tissue Int 1984 Mar;36(S1):S31–S36.

9. *Meunier A.* Scanning acoustic microscope studies of the elastic properties of osteons and osteon lamellae. J Biomech Eng 2008 Mar 17;115(4B):543.

We would like to give my sincere gratitude for the Budapest University of Technology and Economics in the Cooperation Research Center for Biomechanics for the possibility to use the measurement equipments. I would also like to thank Péter Mészáros for his unwavering help and support.

János Simonovics
Budapest University of Technology and Economics, Department of Machine and Product Design
H–1111 Budapest, Bertalan Lajos u. 1–3.
Tel.: (+36) 30 373 66 54

Assessment of a large volume maxillofacial CBCT system – from biomechanical point of view – as a tool to build patient customized bio-models

János Simonovics[1], Péter Bujtár[2], Károly Váradi[1], Attila Szűcs[3], Zsolt Fejér[4]
[1]Budapest University of Technology and Economics, Department of Machine and Product Design
[2]University Hospitals of Oulu, Department of Oral and Maxillofacial Surgery
[3]Semmelweis University, Department of Oro-Maxillofacial Surgery and Stomatology
[4]Semmelweis University, Department of Human Morphology and Developmental Biology
janos@simonovics.hu

Abstract
The number of patients diagnosed with cancer is reaching a scarily high number worldwide. This is no different in the area of mandible cancer. Unfortunately Hungary is quite high up in the ladder. The registered known number of patients with mandible cancer and the associated number of death occurrences are also showing significant data in the country. However it is easy to diagnose, alcohol consumption and smoking or just bad oral hygiene really pushes the statistics. Inside the oral cavity, in case of mandible cancer and late diagnosis the only viable solution is the bone resection.
To determine the extent of the cancer and to carefully plan the surgery procedure or in case of models which were created for biomechanical examinations, the medical science more and more often uses the image based processes and tools. Next to the realistically built models a more punctual mechanical parameter simulation becomes possible.
It is highly important that the necessary information is extracted from the patients with the least stress. With the shortest time and smallest radiation the image must be made in a way that the scan can be well evaluated and it is usable.
Within the current examination in the medical field of imaging methods a gold standard MSCT and a specifically in the head-neck region used CBCT methods will be compared specifically from biomechanical modelling point of view. During the comparison the gray value was examined by the use of a cadaver head.
The results show that the gray values provided by CBCT differs slightly from the MSCT values that is considered as reference. The more extent absolute error occurs with less frequency. Based on these facts the CBCT can be used for the density based material comparison for biomechanical models with less radiation dose.

Keywords: mandible, cadaver, gray value, bone

Introduction

Worldwide the cancer is becoming one of the main problems of our time. It can be found within all the layers of our society. As of the cure there are many question marks. The situation is no different in our homeland, in Hungary either. Unfortunately considering only the oral cavity region, the situation becomes even worse. Hungary has a critically high number of diagnosed oral cavity cancers and the connected occurrence of death. This

bad ranking is generated, although the oral cavity cancer is one of the easiest to detect and diagnose. The screening can be done within a regular dental examination and the control can be done by the family or factory doctor as well. The oral cancer is increasingly present among the people older than 50 years. Potential danger for the development of the cancer is the inadequate food consumption (originated from the lower social status), neglected dental hygiene, alcoholism and smoke. Despite the easy screening possibility a high portion of the patients get diagnosed too late, when the symptoms are causing actual pain. When the mandible is also effected, normally surgery and therefore the dissection of the bone affected by the cancer is unavoidable. This dissection can affect the complete or just partial cross section of the bone. As the result of the surgery the mechanical load carrying capacity of the mandible is changed as well as the self image of the patient.

To determine the exact size of the defect, in the medical field imaging methods are used. Nowadays aside from the varying possibilities the use of CT (Computer Tomography) is becoming more general *(Figure 1)*.

The output from the CT based on the generated image can be very diverse. With and adequate tissue segmenting and based on the extent of the cancer the doctor can make a concrete plan for the surgery, this way drastically reducing the time needed for the surgery and the amount of trauma that will affect the patient.[1–4] The data can be used for biomechanical modelling as well.

The CT method was first used in 1972 in clinical environment. During the imaging the CT uses the X-Ray radiation, which is collected by detectors. The X-Ray radiator and the detectors are also revolving around the patient. The CT, just as the X-Ray, is based on the radiation weakening; however CT can show a radiation weakening of a volume unit more precisely. During the processing one pixel equals to the radiation weakening of a volume unit coefficient, which is than assigned to the gray value. The different tissue domains can be perfectly separated; however the domain that can be seen with bare eyes is very narrow, therefore a windowing method is used.

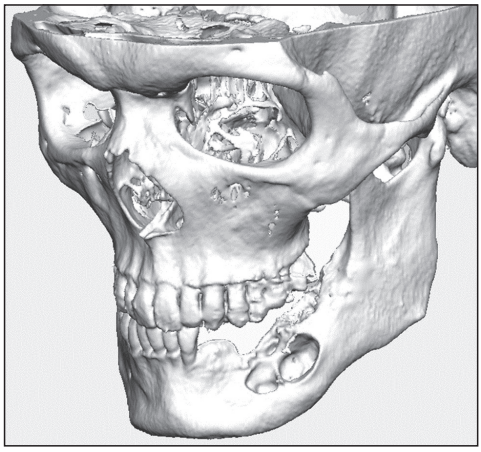

Figure 1. Mandibular tumor

The CBCT (Cone Beam Computer Tomography) is specifically developed tomography for the head-neck region. The picture series is created by tapered radiation beam rays, which is 2 dimensioned and after this the 3 dimension image is created.

Some of the benefits of CBCT are that it is a smaller device; its costs can be 5 times smaller than the traditional medical grade CT (MSCT). Partially this is a reason for the cheaper examination cost as well. It is not necessary to have special mounting, cooling or even electrical infrastructure. It is important to highlight, that during the CBCT examination the radiation load can be 100 times smaller on the patient as in case of the MSCT, even in same or higher resolution. The processing of the image is also faster. Of course with all the

benefits there are some limitations as well that should be considered when using the CBCT, for example the less punctual gray value or the not always optimal hard and soft tissue contrast.

Methods

The goal of this study is a validation and verification with maxillofacial cadaver, in the meaning that a large volume in-office CBCT provides reliable data compared to a medical grade MSCT as a gold standard technology. Based on the gray value that is provided by picturing methods adequate tissue segmenting and material properties with the use of density transfer functions can be defined.[5] This will be specifically important for the geometrical model and later the virtual mechanical simulation as input information source.

For this examination a toothless, in formaldehyde fixated old female cadaver head with 4 approximately 20 mm layer put on each other was used. This was provided by the Department of Human Morphology and Development Biology, Budapest, Hungary. The preparation of the cadaver head was also carried out in the same institute. During preparation of the head in predetermined focus points within the layers known density elements [in 0.93–2.70 g/cm^3 domain], Polyoxymehylene (POM) 1.415 [g/cm^3], Polyethylene (PE) 0.93 [g/cm^3], Borosilicate glass 2.21 [g/cm^3] and aluminum (Al) 2.70 [g/cm^3] were concentrically placed inside and outside of the oral cavity. These elements made the evaluation easier. The elements considering the geometry consisted of 5 mm diameter spheres (aluminum and glass) and 5 mm height and diameter helicons (POM and PE) *(Figure 2)*.

The same sample was scanned with CBCT and MSCT without any change. In case of the CBCT the precision of the device is not satisfactory defined based on the gray value scale. During the examination as reference, a calibrated, seemingly old constructed, 8 layered MSCT (General Electric, LightSpeed Ultra 8, GE Medical Systems, Waukesha, Wis) was selected, which was compared to the

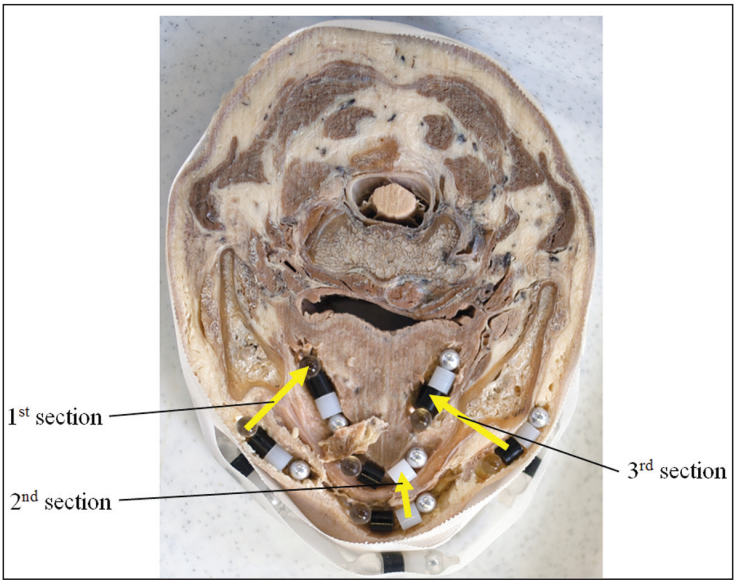

Figure 2. Examined sections on cadaver

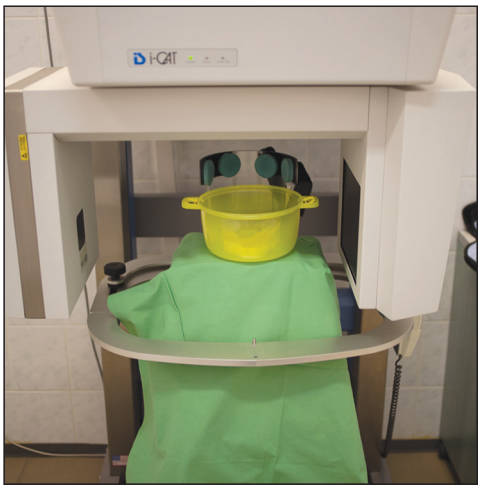

Figure 3. Preparing CBCT scan

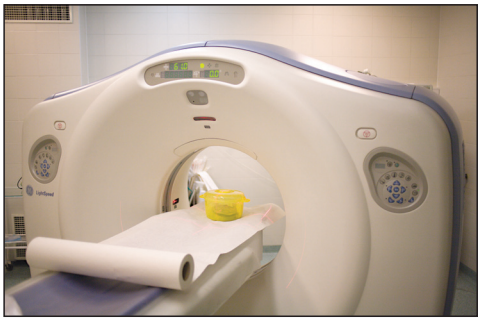

Figure 4. Preparing MSCT scan

CBCT (i-CAT, Xoran Technologies, Ann Arbor, MI) *(Figures 3–4)*.

Exclusively only the parameters used in the clinical practice were considered for the comprehensive examination. This means with 120KeV adaptive acquisition protocol, adjusting the beam current between 160–230 mAs, BONEPLUS algorithm was used for the scanning. The layer thickness in the everyday practice is 1.25–2.5 mm, which is highly important for the radiation hygiene and for the low radiation load of the patient in case of the MSCT. Based on this the layer thickness was defined to be 1.25 mm, 0.488 × 0.488 mm pixel per axial layers with 0.625 pitch. The CBCT with 120 KeV were calibrated with 36 mAs with 0.25 × 0.25 × 0.25 mm spatial resolution.

With these parameters the scanning times and parameters in the clinical practice were represented in case of both devices. These values are important parameters for the patient. During the measurements the comparison of the density data were based on the gray values. The density was measured in function of the distance in 3 randomly selected elements in the linear section in case of both tomographies. The measurement was done between 1-1 identical reference elements in the horizontal plane *(Figure 2)*. After this the results were compared. The cadaver sample after the scanning was delivered back to the Department of Human Morphology and Development Biology (Budapest, Hungary).

Results

During the examination with 3 orientations, sections between 1-1 reference materials were examined in case of both CTs. When examining the sections in predefined 0.25 mm steps, gray values were collected and compared. In the 3 different sections the gray values were graphed in the horizontal plane between same reference elements. With the same step values the differences between the CT considered and graphed with absolute values, the deviation between the devices can be seen very transparently. With the help of absolute differences, their frequency of occurrence was also examined and graphed in a histogram with the relative sum of frequency *(Figures 5–7)*.

From the diagram it can be seen that the average gray value deviation considering the 3 sections is between 72 and 98. It can be further concluded from the histogram of the absolute gray value deviation of the sections, that

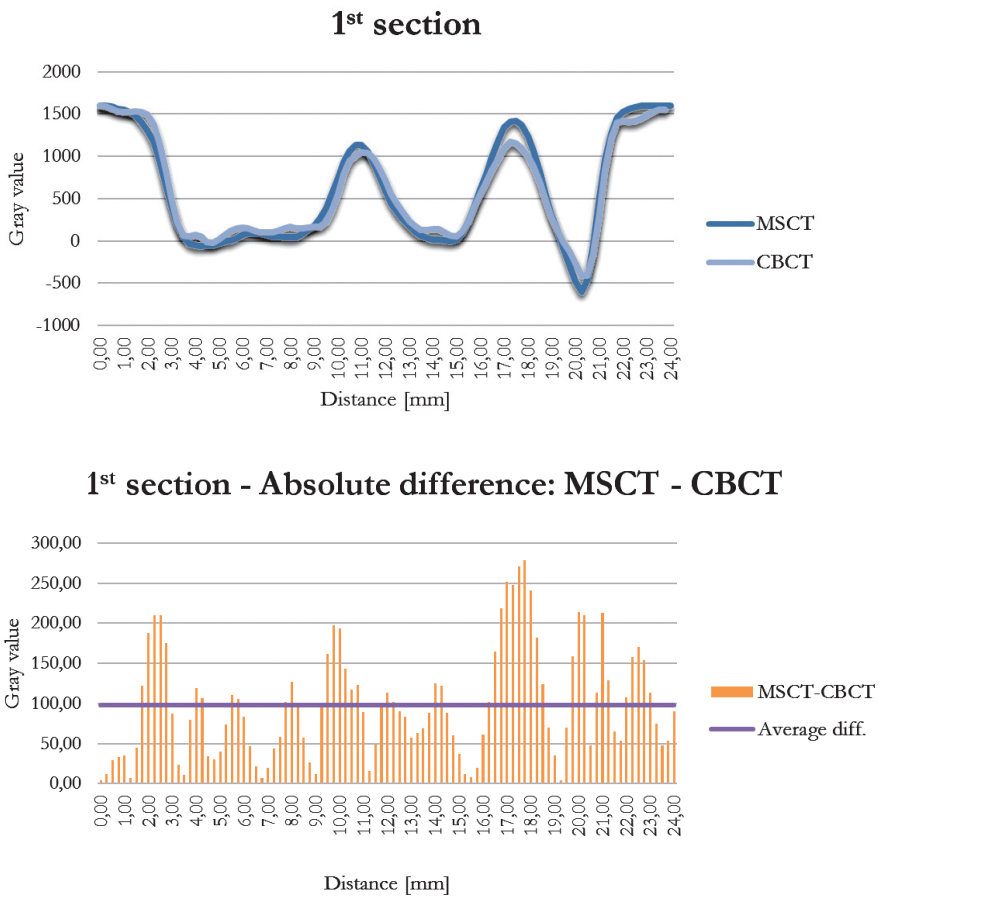

Figure 5. 1st section results

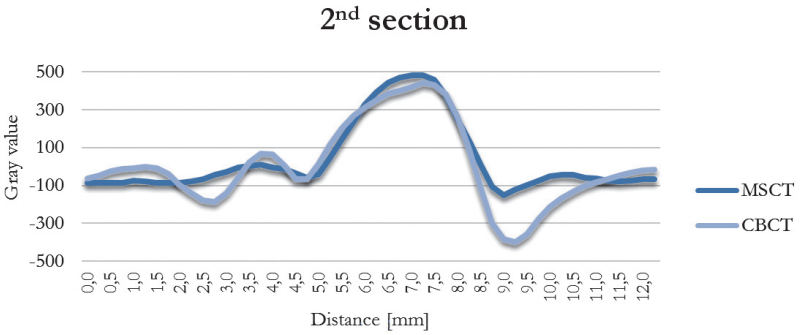

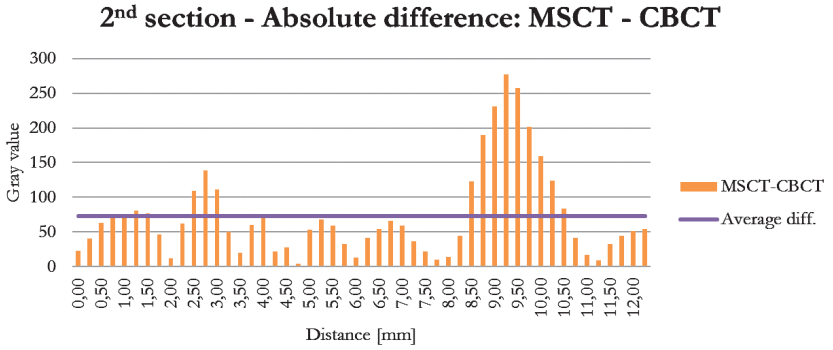

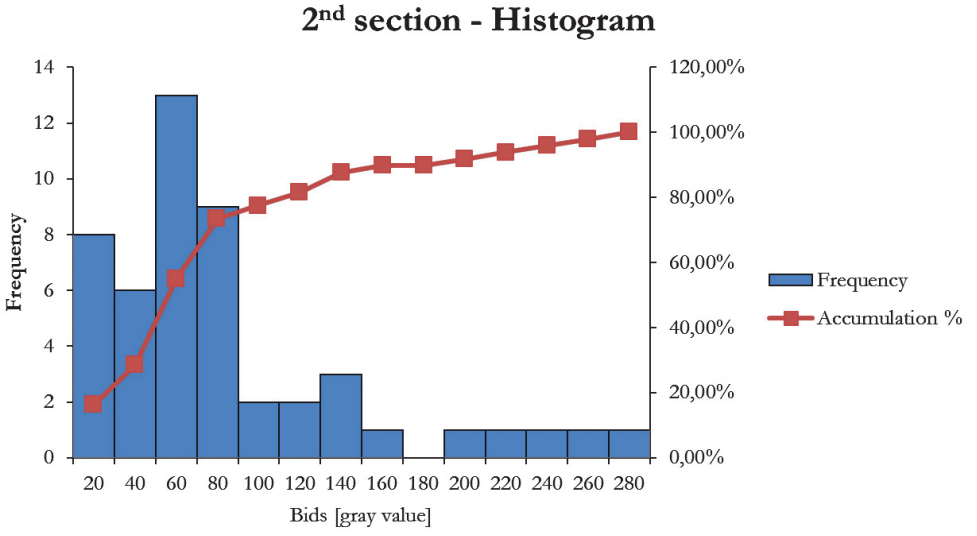

Figure 6. 2nd section results

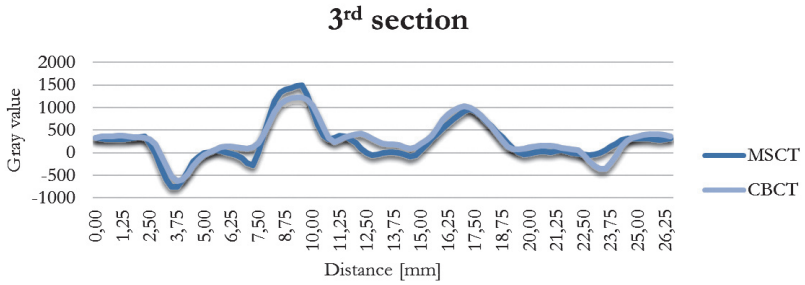

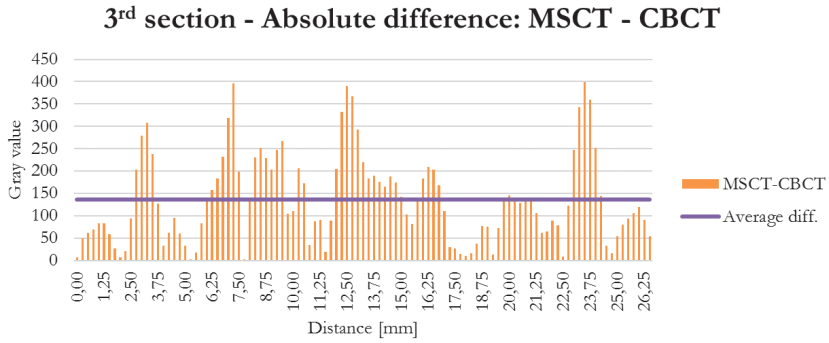

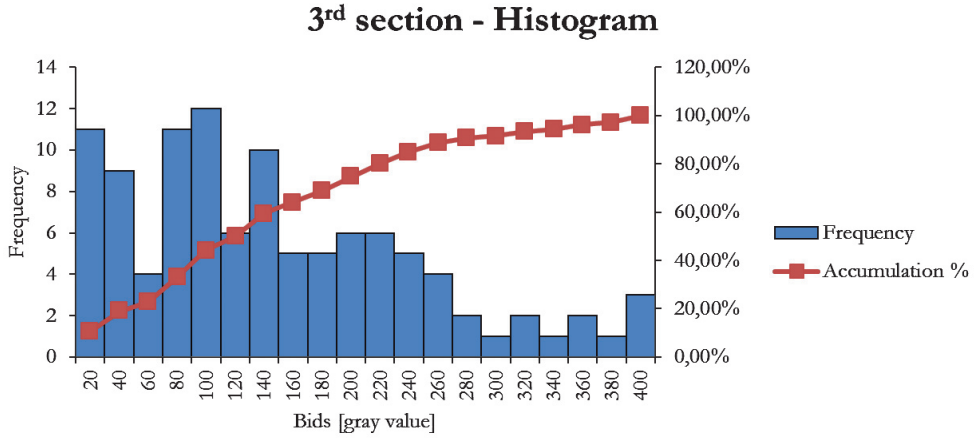

Figure 7. 3rd section results

140 gray value and smaller deviations are more frequently occurring, hence between the two CT the frequency of the higher gray value mistakes is lower *(Figures 5–7)*. Based on the use of both CT with clinical parameters the gray value differences can be attributed to the difference in resolution until a certain level. While MSCT worked with average values with 1.25 mm sections, the CBCT had more values. This concludes that in certain cases in can be more precise.

The gray values are very important for the determination of the density of each allocations. In the field of biomechanical modelling and simulation the definition of material properties with density based transfer functions provided by imaging methods are becoming more and more popular based on the current state of the art. These models can be more precise for biomechanical simulations.[6,7] The CBCT output data compared to MSCT (gold standard) can be adequate for biomechanical modelling, further considering that in case of the patient the radiation load can be 100 times smaller and the cost is also reduced. The differences between the two CTs during the creation of the simulation models with the mechanical parameters setting make little deviation.

Summary

In the research two devices used in the medical field, the MSCT and CBCT were compared considering clinical parameters with the use of cadaver human head applied with reference elements. During the examination the CTs were compared based on the gray values. The deviation of the gray values provided by the CBCT is rather small compared to the MSCT that is considered as reference. Based on these facts it can be concluded that the CBCT can be used for material comparison during the biomechanical modelling with transfer functions used on the gray values.

References

1. *Zheng G, Su Y, Liao G, Chen Z, Wang L, Jiao P, et al.* Mandible reconstruction assisted by preoperative virtual surgical simulation. Oral Surg Oral Med Oral Pathol Oral Radiol 2012 May; 113(5):604–11.

2. *Wang WH, Zhu J, Deng JY, Xia B, Xu B.* Three-dimensional virtual technology in reconstruction of mandibular defect including condyle using double-barrel vascularized fibula flap. J Cranio-Maxillofac Surg 2013 Jul;41(5):417–22.

3. *Thomas CV, McMillan KG, Jeynes P, Martin T, Parmar S.* Use of a titanium cutting guide to assist raising the composite radial forearm free flap. Int J Oral Maxillofac Surg [serial online]. 2013 Aug[cited 2013 Sept 20]. Available from: URL: *http://linkinghub.elsevier.com/retrieve/pii/S0901502713002932.*

4. *Seeberger R, Scherfler S, Freier K, Thiele O.* Use of stereolithographic cutting guides in corrective (wedge) Lefort I osteotomy. Br J Oral Maxillofac Surg 2011;49(5):e20–e1.

5. *Rho JY, Hobatho MC, Ashman RB.* Relations of mechanical properties to density and CT numbers in human bone. Med Eng Phys 1995; 17(5):347–55.

6. *Chen G, Schmutz B, Epari D, Rathnayaka K, Ibrahim S, Schuetz MA, et al.* A new approach for assigning bone material properties from CT images into finite element models. J Biomech. 2010 Mar; 43(5):1011–5.

7. *Schileo E, Dall'Ara E, Taddei F, Malandrino A, Schotkamp T, Baleani M, et al.* An accurate estimation of bone density improves the accuracy of subject-specific finite element models. J Biomech 2008 Aug;41(11):2483–91.

We would like to show my appreciation to Dr. Gábor Forrai to provide me the possibility to have the measurement on the MSCT device (Head of Department of Radiology, National Health Center, Budapest, Hungary). I would like to give my full hearted thanks to Barbara Bell (Department of Radiology, National Health Centre, Budapest, Hungary) and Katalin Bády specialist radiographers for the help they provided during the scanning process. Last but not least I would like to send my special thanks to Péter Mészáros for his unwavering help and support.

János Simonovics
Budapest University of Technology and Economics, Department of Machine and Product Design
H–1111 Budapest, Bertalan Lajos u. 1–3.
Tel.: (+36) 30 373 66 54

Biomechanica Hungarica VII. évfolyam, 2. szám

Numerical investigation of the hemostasis process in transient blood flow

Gábor Závodszky, György Paál
Budapest University of Technology and Economics, Department of Hydrodynamic Systems
gzavodszky@gmail.com

Abstract
Thrombus formation is a thoroughly researched area, posing several unanswered questions. Quite many of the underlying processes are still not well understood. This uncertainty arises from the fact that the blood clotting mechanism in our bodies involves a rather complex reaction cascade with plenty of components. These underlying dynamic processes stretch over the domains of several disciplines (as there are biomechanical and biochemical reactions as well as fluid dynamical components). In this study the factors thought to be the most influential were selected and coupled with the transient flow field that reacts not only to the cardiac pressure waves but also to the changing geometry of the vessel due to the clot formation. Although the number of degrees of freedom is reduced heavily, this model is already capable of qualitatively reproducing the results of in-vivo measured hemostasis.

Keywords: coagulation, platelets, computational fluid dynamics

Introduction

The cascade process of the hemostasis is a vital self-defense process exhibited by our body. This is a natural response of the cardiovascular system that prevents undesirable blood loss in case of vascular injury. The blood coagulation is an important step during the hemostasis and its highly complicated cascade process is driven by several factors that can act either as a promoter or an inhibitor. The main steps include the aggregation and the binding of the platelets that are dependent on the local flow properties amongst other circumstances. Simulating this aggregation phenomenon is a challenging task as one has to make several appropriately chosen approximations. Anand et al. reviewed[1] some of the interacting mechanisms regarding clot formation in flowing blood, and even though they deal with a narrower collection of participating processes than it is known in the current literature, from the view of a numerical simulation they are still numerous. Nesbitt et al. provided[2] some more insight into the thrombus formation by emphasizing the strong coupling between the biochemical processes and the local hemodynamic properties. According to their experimental work, platelet aggregation is influenced by emerging shear forces as platelet adhesion favours low-shear zones. Several other authors recorded the ongoing process of thrombus formation: for example Celi et al. recorded[3] the thrombus formation in the microcirculation of a living mouse using wide-field video-microscopy. Similar measurements were carried out using different reagents to highlight the concentration of the main components of the formation.[4,5] While the number of high quality recording of this phenomena is increasing, the numerical simulations are still in a rather early stage. There are several pieces of work aiming at simulating thrombus formation numerically, but most of them cover only portions of the whole process.[6–9] They try to solve the complex problem by approaching it either from the biochemical side and com-

pute the reactions and the densities of the reagents, but fail to couple these equations with the transient (time-varying) flow field, or from the kinetic side, which usually lacks the appropriate handling of platelet concentrations. The platelet concentration profile inside the blood vessels is an important factor, which is far from being constant in either venous or arterial vessels.[10] A lot of numerical models have been developed in the past decade in order to calculate the platelet concentration profile.[11–13] Their main findings are that the marginating property of platelets is mainly caused by the finite size effect of both the smaller platelets and the significantly larger red blood cells (RBC). Technically the rolling motion of the larger RBCs pushes the platelets to the sides of the flow channel, thus creating a highly uneven platelet distribution across the diameter of the vessels. This drift force that acts upon platelets in blood flow seems to be proportional to the average local flow velocity. To prove this interaction between platelets and RBCs, Mountrakis et al. simulated[14] particle collisions in blood flow using the immersed boundary method.

Method

During our simulations the blood coagulation mechanism made the geometry change in time. For this reason a two-dimensional lattice Boltzmann based fluid solver was implemented on a typical D2Q9 lattice to carry out the computations. This fluid solver method has a clear advantage in handling complex and changing geometries over the more conventional finite-volume solvers. The theoretical bases of this method were laid down by Bhatnagar, Gross and Krook (BGK),[15] and were later developed to the level of general usability for fluid flows by Quian et al.[16] We employed the so-called multiple-relaxation-time lattice Boltzmann model,[17] which, for our case provided increased numerical stability compared to the widely used BGK model.

The platelets immersed in the blood flow were simulated as a passive scalar concentration field. The passive attribute means that although the platelet distribution is driven by the pulsating blood flow, it has no influence back on it. This approximation is supported by the fact that the usual volumetric ratio of the platelets in blood is under 1%. The advection-diffusion of these platelets was handled by the LBM method in the following way: when the velocity is prescribed by an already given velocity field (like in this case by the blood flow), the equilibrium function (from the original function[16]) of the scalar field reduces to the following:

$$f_i^{eq} = \omega\rho(1 + 3\vec{e_i} \cdot \vec{u}) \tag{1}$$

where ω is the relaxation frequency, $\vec{e_i}$ is the *i*-th discretized velocity direction, $\vec{u}$ is the local velocity of the blood flow, and is the platelet concentration that can be computed analogously to fluid density:

$$\rho = \sum_{i=1}^{9} f_i \tag{2}$$

where f_i is the particle distribution along the *i*-th discretized velocity on the lattice. The diffusion coefficient *D* then analogous to the numerical viscosity:

$$D = \frac{1}{3}(\tau - \frac{1}{2}) \tag{3}$$

where $\tau = \frac{1}{\omega}$ is the relaxation time for the equilibrium function.

To acquire a proper platelet density profile, the interaction with the RBCs must be taken into account. The platelet drifting is mainly caused by the rolling motion of the RBCs, which is in turn caused by the emerging shear forces in the fluid. To simulate this marginating effect, a virtual force $\overrightarrow{F_M}$ has been prescribed that acts

upon the density of the platelets. This force actually accounts for the finite size effects of the platelets and RBCs. The drift force acting on real platelets always drives platelets out from the main flow, to the sides of the vessel. It is a required behavior, as this causes increased platelet concentration in the vicinity of vessel walls where any injury can possibly occur. This $\overrightarrow{F_M}$ force points to the direction of the local largest shear stress decrease (in other words, to the direction of the smallest, most negative shear stress gradient). Its magnitude is proportional to the magnitude of the shear stress emerging in this specified direction. (We note here that this proportionality ratio will require a proper parameter study later. In the current work, it takes the value of unity.) Using this drift force, two simple channel flows were simulated with Reynolds numbers that are typical in these smaller vessels. The vessel wall was taken as a smooth, no-slip, rigid wall. The results of the simulations were compared to the experimental results of Woldhuis et al.[16]

The first simple channel flow simulation used constant velocity inlet and constant pressure outlet boundaries. The Reynolds number was set to one that is a typical value in venules. The result of the simulation is summarized below in *Figure 1*.

The platelet concentration shows a good qualitative agreement with the experimental results. This numerical model was tested with pulsatile flow as well, in order to reinforce the statement of its validity. For this reason, the other simulation used a time-varying inlet velocity boundary condition. *Figure 2* shows the inlet flow rate profile that mimics the behaviour of a real cardiac pressure wave.

The Reynolds number defined with the maximum of the possible inlet velocity was set to ten, which is a usual value for arterioles. The results of the simulation were also compared

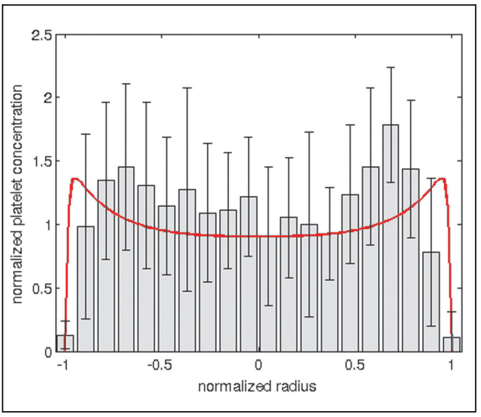

Figure 1. Normalized platelet concentration profile in a venule. The continuous red curve shows the results of the stationary simulation plotted over the experimental results of Woldhuis et al.[18] (Re=1)

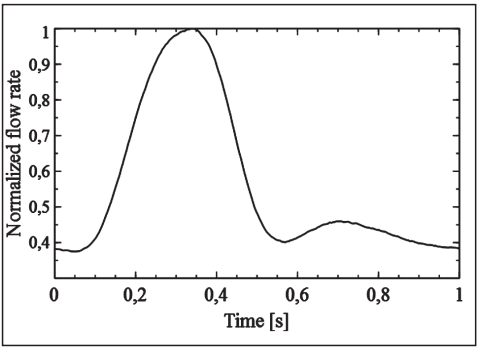

Figure 2. Normalized artificial flow rate curve that mimics the behaviour of a real flow rate curve during a cardiac cycle

to the experimental results of the same authors in *Figure 3*. Again, good qualitative agreement was found. The biggest deviation between the simulation and experimental results can be found very close to the vessel walls but it is still within the error bars.

The coagulation of blood is modeled by changing the type of a numerical element from fluid cell to solid cell. For the thrombus formation in our simulation, coagulation is only possible at sites right next to vessel walls or next to rigid

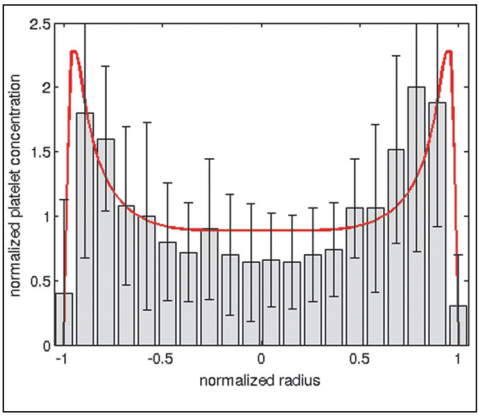

Figure 3. Time-averaged normalized platelet concentration profile in an arteriole. The continuous red curve shows the results of a transient simulation plotted over the experimental results of Woldhuis et al.[18] (Re=10)

blood cells that have already come to stasis. All the fluid LBM cells next to a wall cell were tracked, as these cells have the ability to turn into a solid cell themselves. When this happens, their fluid cell neighbours are added to the list of near-wall cells. Though platelet activation in reality is a complex cascade process, we only simulate one reagent, the adenosine diphosphate (ADP) concentration that is in our simulation not coupled with the blood flow. This means that the ADP concentration is not influenced by the local flow properties directly. When a platelet is activated (or in our simulation when coagulation of a numerical lattice happens), it releases ADP that can initiate the activation of other platelets. In the simulations the ADP concentration decreases exponentially in space, so its release can be thought of as a local ADP concentration increase.

Coagulation at a numeric lattice site is dependent on the relation of three variables:

$$P_{coag} = \frac{\rho_{platelet} \cdot \rho_{ADP}}{\tau_{MAX}} \qquad (4)$$

where the P_{coag} is a probability in the sense, that its value decides whether a fluid cell should come to stasis or not at any given time, based on the current local platelet concentration $\rho_{platelet}$, the local ADP concentration ρ_{ADP}, and the local maximum shear component of the stress tensor denoted by τ_{MAX}. The threshold level of P_{coag} that a numerical lattice has to reach for coagulation is an empirical parameter of the model for now. A later work should explore the deeper relation of these parameters. For a numerical fluid cell to come to stasis the parameters have to remain in the coagulation zone for a t_{window} time. This time-window was chosen to be $t_{window} = 20\ ms$ because this is the usual timeframe for ADP to activate a platelet. This also means that a newly registered near-wall lattice cannot turn into a solid cell sooner than *20 ms*.

Results

In *Figure 4* a visualized snapshot of a coagulation simulation is shown after six heartbeat cycles. The formation of the thrombus starts at an injury site. In in-vivo systems in case of vascular injury, a significant amount of ADP is released into the bloodstream from the injured vessel wall tissue. The injury site in this case was simulated by increasing the ADP concentration at a small amount of numerical lattices along the vessel wall. There are a few qualitative features of the calculated thrombus that should be mentioned. Firstly, as the thrombus begins to block the flow channel, the velocity increases and that leads to larger emerging shear stresses that inhibit the process of the coagulation. This results in the relatively flat top of the thrombus. It is also noticeable that the thrombus growth is asymmetric to the site of injury; its growth is slower on the side facing the incoming bloodstream. This is again the result of the different shear stresses.

The simulation results were compared to two thrombus geometries recorded at different times with video-microscopy by Nesbitt et al.[10]

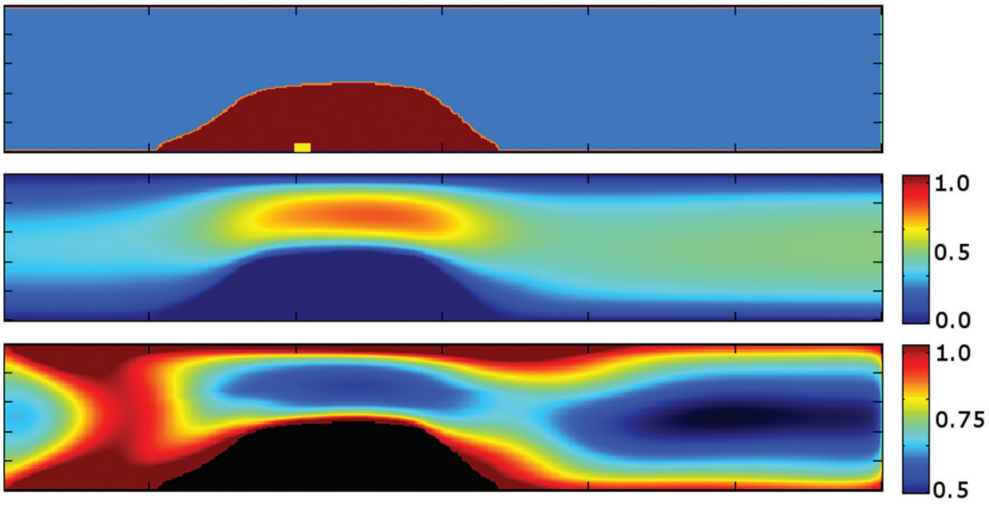

Figure 4. Typical result of a thrombus formation simulation at time instant of the end of a heartbeat cycle. The flow direction is from the left to the right. The upper image shows the emerged geometry of the thrombus, with the place of vessel injury (yellow box at the bases of the thrombus). The middle image shows the current normalized velocity magnitudes (Reynolds number equals 10). The lower image shows the normalized platelet concentration at the same instant

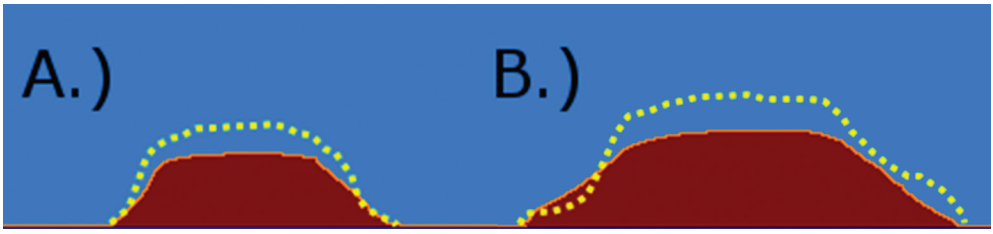

Figure 5. Geometry of the thrombus after three A.) and after six B.) heart beat cycles. The yellow dotted outline shows the geometry of the thrombus recorded with video-microscopy by Nesbitt et al.[2]

in *Figure 5*. The experimental results originate from an induced injury inside the arteriole of a living mouse. The exact form of the thrombus naturally depends on much more components that are taken into account in the current numerical simulation. Still, some qualitative features like effects of shear stresses can be studied with it.

Conclusions

Hemostasis is a heavily studied topic that represents deep complexity. The aim of a numerical simulation is to reproduce certain features of a phenomena using the smallest necessary state space. In this work a numerical model was presented for hemostasis that incorporates different contributing disciplines in a computationally effective way. And though this model evidently has some shortcomings, like that in a real thrombus the outer layer is often not solid, and can dissolve easily in the flow and subside again later. In our model, however, the thrombus is handled as solid material, unable to dissolve. The effects of the several other components of the coagulation cascade were

not taken into account either. Still, according to the comparison these key components coupled with the blood flow seems to be sufficient to reproduce the major characteristics of an injury induced thrombus. It should also be mentioned that due to the strongly simplified nature of the model, it might be capable of simulating other sediments in blood flows, like the deposition of fat particles on clinical devices.

References

1. *Anand M, Rajagopal KR.* A model incorporating some of the mechanical and biochemical factors underlying clot formation and dissolution in flowing blood. Journal of Theoretical Medicine 2003;5:183–218.

2. *Nesbitt WS, Westein E, Tovar-Lopez FJ, Tolouei E, Mitchell A, Fu J, Carberry J, Fouras A, Jackson SP.* A shear gradient-dependent platelet aggregation mechanism drives thrombus formation. Nature Medicine 2009;15:665–73.

3. *Celi A, Merrill-Skoloff G, Gross P, Falati S, Sim DS, Flaumenhaft R, Furie BC, Furie B.* Thrombus formation: direct real-time observation and digital analysis of thrombus assembly in a living mouse by confocal and widefield intravital microscopy. Journal of thrombosis and haemostasis 2003;1(1):60–8.

4. *Falati S, Gross P, Merrill-Skoloff G, Furie BC, Furie B.* Real-time in vivo imaging of platelets, tissue factor and fibrin during arterial thrombus formation in the mouse. Nature Medicine 2002;8:1175-81.

5. *Furie B, Furie BC.* In vivo thrombus formation. Journal of thrombosis and haemostasis 2007; 5(1):12–7.

6. *Alenitsyn AG, Kondratyev AS, Mikhailova I, Siddique I.* Mathematical modeling of thrombus growth in microvessels. Journal of Prime Research in Mathematics 2008;4:195–205.

7. *Harrison SE, Smith SM, Bernsdorf J, Hose DR, Lawford PV.* Application and validation of the lattice Boltzmann method for modelling flow-related clotting. Journal of Biomechanics 2007; 40:3023–8.

8. *Wang W, King MR.* Multiscale modeling of platelet adhesion and thrombus growth. Annals of Biomedical Engineering 2012 Nov;40(11) 2345–54.

9. *Tamagawa M, Kaneda H, Hiramoto M, Nagahama S.* Simulation of thrombus formation in shear flows using Lattice Boltzmann Method. Artificial Organs 2009;33:604–10.

10. *Zhao H, Shaqfeh E. SG.* Numerical simulation of the margination of platelets in the microvasculature. Center of turbulence research, Stanford, Annual Research Briefs 2010.

11. *Jordan A, David T, Homer-Vanniasinkam S, Graham A, Walker P.* The effects of margination and red cell augmented platelet diffusivity on platelet adhesion in complex flow. Biorheology 2004;41:641–53.

12. *Tokarev AA, Butylin AA, Ermakova EA, Shnol EE, Panasenko GP, Ataullakhanov FI.* Finite platelet size could be responsible for platelet margination effect. Biophysical Journal 2011; 101:1835–43.

13. *Zhao R, Kameneva MV, Antaki JF.* Investigation of platelet margination phenomena at elevated shear stress. Biorheology 2007;44:161-77.

14. *Mountrakis L, Hoekstra LE, Hoekstra AG.* Where do the platelets go? A simulation study of fully resolved blood flow through aneurysmal vessels. Interface Focus 3: 20120089, Royal Society Publishing 2012.

15. *Bhatnagar PL, Gross EP, Krook.* A model for collision processes in gases. I. small amplitude processes in charged and neutral one-component systems. Physical Review 1954;94:511–25.

16. *Qian YH, D' Humières D, Lallemand P.* Lattice BGK models for Navier-Stokes equation. Europhysics Letters 1992;17:479–84.

17. *D'Humières D, Ginzburg I, Krafczyk M, Lallemand P, Luo LS.* Multiple-relaxation-time lattice Boltzmann models in three dimensions. Philosophical Transactions of the Royal Society – Series A: Mathematical, Physical and Engineering Sciences 2002;360:437–51.

18. *Woldhuis B, Tangelder GJ, Slaaf DW, Reneman RS.* Concentration profile of blood platelets differs in arterioles and venules. American Journal of Physiology 1992;262:H1217-H23.

Gábor Závodszky
Budapest University of Technology and Economics, Department of Hydrodynamic Systems
H–1521 Budapest, Pf. 91.
Tel.: (+36) 1 463-1111/5798

Biomechanica Hungarica VII. évfolyam, 2. szám

Estimation of moments acting on the pelvis in standing and in two different sitting postures

Bálint Héra, József Zalavári
Budapest University of Technology and Economics, Department of Machine and Product Design
hera.balint@gt3.bme.hu

Abstract
According to popular consideration prolonged sitting posture in work can cause pain at different regions of the back. Many researches aiming to define the relationship between these two, and as a result of noticing the problem many design solutions can be found, some of which are considered as alternative. Healthy sitting posture should be mean that with anterior rotation of the pelvis the curve of the lumbar spine would be neutral or more preferably lordotic. In sitting the muscle balance changes thus there is more muscle activity needed for erection of the trunk and anterior rotation of the pelvis. In this study muscle activity in standing and in two different sitting postures is estimated as a difference of the two moments acting on the pelvis, which are the upper body weight moment and the passive elastic moment. Further investigation of the effects of hip-flexing thigh muscles or other passive tissues on pelvic range of motion is warranted.

Keywords: sitting biomechanics, standing, passive moment, active moment, weight moment, hip joint angle

1. How sedentary work style affects health

1.1. Sitting at work

Sitting posture is more preferably during activities in that changing the place is not necessary. Under constant loading, those thigh and trunk muscles that keeping the upper body in an erect posture can be exhausted. Sitting on a chair the upper body weight is supported by the seat so that many of the muscles are relaxed. Most of the craftsmen were on the spot, just like today's office workers and computer workers. Driving car, watching TV and using PC we spent additional hours sitting after official work time.

The harmful effects of a sedentary work style were first described around 1700 by the Italian physician Bernardino Ramazzini who considerably grounded occupational medicine. "Those who sit at their work and are therefore called 'chairworkers,' such as cobblers and tailors ... become bent, humpbacked, and hold their heads down like people looking for something on the ground; this is the effect of their sedentary life (…)".[1] Besides craftsmen he also mentioned clerks. Ramazzini was the first who established that the constant sitting posture is among risk factors of diseases, and he noticed all chairworkers are suffering lumbago. The classic word lumbago refers to a sudden pain arising around the lower back and the sacrum, which warns to the overload or functional mismatch of the lower spine.[2] There are many today's examples for occupational sitting, such as occupational driving or different office jobs. The latter is spreading, engineers, physicians and managers spending hours in front of the computer. Growing attention is paid to the back pain and body postures of school children.

1.2. Consequences of prolonged sitting posture

According to popular consideration prolonged sitting posture in work can cause pain at different regions of the back. In my research possible evading of low back pain is examined. Low back pain (LPB) is the type of back pain arising at the sacrum and lumbar vertebras. Causes of mechanical low back pain are important. These are for example the non-specific injuries of the musculoskeletal system; herniated discs; compressing of nerve roots; degenerative changes in the intervertebral disc or joint; fracture of the vertebrae; injury of muscles and ligaments; etc. Low back pain is a serious health issue in the developed countries with over half of sedentary workers reporting LBP during their lifetime.[3]

There is a debate among researchers about the relationship between sitting posture and pain sensed in the back. Some studies demonstrated associations between a history of sedentary work, low-back pain prevalence and degenerative changes of the intervertebral disc.[4,5] However, other studies do not found such relationship.[6,7] In their review of studies which are examining the connection between occupational sitting and low back pain Lis and colleagues[8] found that sitting by itself does not increase the risk of LBP. However, sitting for more than half a workday in combination with awkward posture does increase the likelihood of having LBP. They also found that awkward posture itself is a risk factor. Opposite to these results, duration of prolonged sitting was considered important by many researchers. Spyropoulos and colleagues[9] studied the prevalence of back pain among Greek public office workers. They have revealed that among significant determinants for predicting LBP occurrence are clerk body position while sitting and sitting time of greater than 6 hours. Janwantanakul and colleagues[10] developed a risk score to identify office workers likely to have LBP. During data collection for the score called The BROW (The Back pain Risk score for Office Workers), respondents were asked about whether they continuously sat or stood for more than two hours a day. Studying Iranian office workers, Razee and colleagues[11] conclude that sitting work style more than four hours had a positive association with increased likelihood of occurrence of LBP.

The great prevalence of back pain in office workers could indicate relationship between sedentary work style and LBP. In the study of Razee and colleagues lifetime prevalence of back pain was 91.2%, and this result for last twelve month was 37,3%. Considering the preceding 12 month of their study, Griffiths and colleagues[12] reporting a 70% lifetime prevalence of LBP for people who spent working with computer more than eight hours a day.

2. Sitting posture and pain

How the musculoskeletal system changes when sitting down, and what is the relationship between these changes and pain sensation at the lower back? Answering this we have to examine human body at the level of its anatomical units. One function of the pain is to call attention to the possibility of an injury. In case of the musculoskeletal system the muscles and ligaments are those that can generate pain via nerve roots. When sitting down, the rotation of specific bones related to each other *(Figure 1)* effects two important changes. First, the arrangement of the lumbar spine changes which is followed by the changes of the loading properties of the soft tissues connecting to it and, in extreme conditions, injury. Second, the muscle equilibrium changes, therefore restoration of the neutral lumbar spine shape needs more muscle activity, which is followed by the changes of the loading properties of the mus-

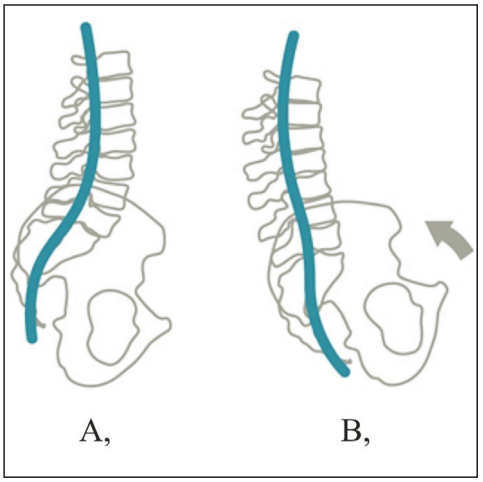

Figure 1. Pelvic position and curvature of the lumbar spine in standing A,) and in sitting with a hip joint angle of 90° B,) (Figure is adapted from Stumpf and Walker[13])

cles, too. Summing up what has been said, pain can frequently arise in soft tissues or in the muscles erecting the trunk or flexing the hip. These muscles are some of the back muscles erecting the trunk (erector spinae, multifidus lumborum), the quadratus lumborum muscle and the iliopsoas muscle which flexing the hip.

With RTG traces Keegan[14] represented posterior rotation of the pelvis in sitting compared with standing which is followed by flattening or dependent on the posture even forward flexing (kyphosis) of the lumber curve. Keegan considered kyphosis as harmful for the lumbar intervertebral disc, however, others reported the beneficial influence of lumbar kyphosis. Harrison and colleagues[15] noticed that in kyphotic position of the lumbar spine a greater amount of intradiscal pressure can be experienced that can cause degeneration of the lumbar intervertebral disc. In kyphosis the shear force pulls the disc posterior possibly leading to the bulging of the disc which can contact the sensitive ligaments and nerve roots by generating pain.

3. Passive moment acting on the pelvis

There are three main moment acting on the pelvis: active moment, passive moment, and the moment comes from the upper body weight. The active moment is caused by the conscious muscle activity for conscious moving or counterbalancing a joint. The passive moment comprises the muscle passive resistance against the rotation of a joint, and the resistance of other soft tissues such as tendons.[16] The pelvis supports the weight of the upper body portion transmitted by through the spine at the sacroiliac joint. The acting line of the body weight does not intersect the hip joint rotation center therefore it causes a moment on the pelvis.

Riener and Edrich[17] examined the resistance of lower extremities against moment which they considered as the passive elastic moment of the hip joint which can be seen as equivalent to the passive moment acting on the pelvis. In their experimental study *(Figure 2)* they have the subject lying supported with a horizontal surface under the back so the legs can be moved. They lifted one segment of a joint of the limb through a dynamometer while the considered joint angle was measured with an electro-gorniometer and other joints were fixed. Total moment of the joint was calculated from the force F measured and the l distance of the cell from the estimated joint center of rotation. This moment consists of a passive elastic and a passive dissipative moment, as well as a dynamic moment caused by inertial effects, and a moment of the gravity acting on the legs.[17] The dissipative moment is caused by the viscoelastic properties of muscles. The limb was moved very slowly (quasi-statically) so that any dynamic effects are negligible. The gravitational moment was calculated from the mass m and the center of gravity l_{COG} of limbs and orthosis distal to the joint investigated. According to these considerations, the passive

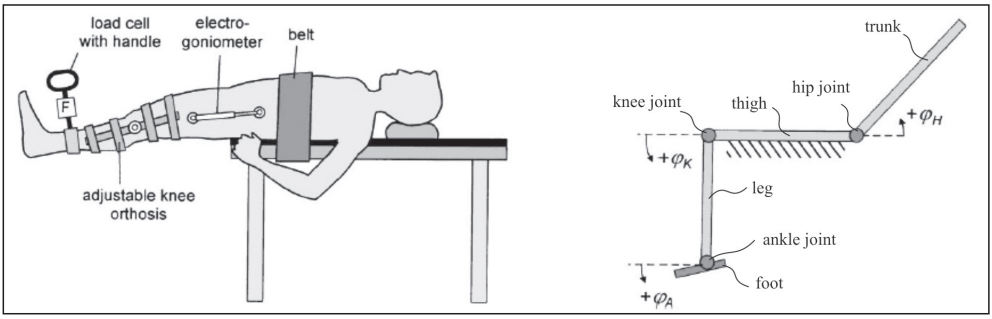

Figure 2. Experimental setup for measuring the passive hip joint moment versus joint angle. The adjacent joint angles were fixed with an adjustable, knee orthosis, or a backrest. The goniometer for measuring joint angles is comprised of two potentiometers connected by a telescopic arm (Murray, 1992). Geometric definitions are illustrated in the right (Figure adapted from Riener and Edrich with permission)

(elastic and dissipative) moment of a joint can be calculated as:

$$M_{pas} \approx Fl\text{-}mgl_{COG}\sin(\varphi\text{-}\varphi_r), \quad (1)$$

where g is the amount of gravity, φ is the joint angle and φ_r is the resting angle, where legs are hanging vertical.

From the measurements of ten subjects using the least square method they defined three so called double exponential function which describe the passive elastic joint moment of the hip, knee and ankle of a generic subject. One of their function with which passive elastic moment of the hip can be calculated[17] is:

$$M_H = \exp(1.4655 - 0.0034\ \varphi_K - 0.0750\ \varphi_H) - \exp(1.3403 - 0.0226\ \varphi_K + 0.0305\ \varphi_H) + 8.072 \quad (2)$$

Where φ_K is the knee joint angle and φ_H is the hip joint angle *(Figure 2)* both in degrees. In *Figure 3* hip joint moment in three different knee angle arrangement is shown.

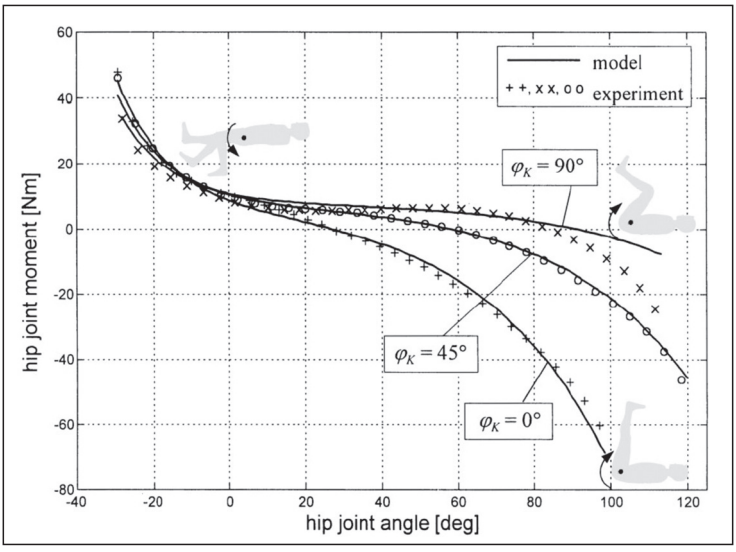

Figure 3. Measured hip joint moment versus hip angle in different knee positions (adapted from Riener and Edrich with permission)

4. Moments calculated in this study

In standing both knee and hip joint angle are 0° while in the popular perpendicular sitting position both are about 90°. Besides these postures there is another sitting posture we can often meet which is considered as alternative. To these three positions passive elastic joint moment and upper body weight moment acting on the pelvis was calculated and as a different of these two active muscle moments was estimated.

4.1. The passive elastic moment of the hip joint

The passive moment calculated with the (2) double exponential function given by Riener and Edrich are shown in *Table 1.* The positive amount of the moment in case of each posture means that the passive moment has a sagittally forward rotating effect on the pelvis. This moment together with the active muscle moment compensate the moment of the upper body weight. With an increase of the hip joint angle there is an increase in the passive moment and an increase active moment is needed to compensate body weight moment. In case of hip joint angle of 90° the passive moment is around zero thus the pelvis and the upper body are stabilized with active muscles.

	1.		2.		3.	
	hip	knee	hip	knee	hip	knee
angle [°]	0	0	45	45	90	90
M_{pas} [Nm]	8.6		2.7		0.3	

Table 1. Passive elastic moment acting on the pelvis (hip join) in three different body postures

4.2. Upper body weight moment

The load of the upper body weight was substituted with a vertical force acting at the center of the sacroiliac joint. This force can be substituted with the L5-S1 joint force given in the study of Arjmand and colleagues[18] who published data calculated with two different model. The single-level optimization-assisted EMG-driven (EMGAO) model contains a process in which the three different components of the joint are estimated with the optimization of preliminary estimated EMG-driven trunk muscle force. The multi-level kinematics-driven (KD) model is a finite element model for a specific part of the musculoskeletal system which contains rigid solid beam elements providing the cumulated nonlinear stiffness and load-displacement relationship of the joint segments.

There is a difference in magnitude of moment arms in case of the three mentioned body posture because the rotation axis of the pelvis changes. In standing position the axis of rotation of the pelvis intersects the center of rotation of the two hip joints while in sitting this axis is defined by the connecting points of the ischial tuberosities and the seat surface. The magnitude of moment arm is given by the length of the transverse section which connects the acting line of the upper body weight to the rotation axis of the pelvis.

The angle of pelvic tilt (PT) for standing and 90° sitting was given by Endo and colleagues.[19] For the calculation of PT in the 45° sitting posture it was estimated that the magnitude of pelvis rotation is half of the magnitude of pelvic rotation between standing and 90° sitting posture. For the calculation of a vectors between two anatomical points of the pelvis and their lengths and their angle in relation to each other *(Figures 4–7),* coordinates data were given from the study of Reynolds and colleagues[20] who measured the pelvis in a tilt angle related to the natural standing body posture and divided the measurements into three anthropometric group (small female, medium male and large male).

The upper body weight moments related to the three postures are:

$$M_{st}=F_i*k_{st} \quad (3)$$

$$M_{si,\,45°}=F_i*k_{si,45°} \quad (4)$$

$$M_{si,90°}=F_i*k_{si,90°} \quad (5)$$

where M_{st} and k_{st} are upper body weight moment and the moment arm in standing position, respectively; $M_{si,\,45°}$ and $k_{si,\,45°}$ are upper body weight moment and moment arm in 45° sitting position, respectively; and $M_{si,90°}$ and $k_{si,90°}$ are upper body weight moment and moment arm in 90° sitting position, respectively. The index *i* relates to the model type KD or EMGAO that have been used for calculating the force. In function 3, 4, and 5 each *k* is the lever arm, where

$$k_{st}=\sin\varphi_{st}*|\underline{d}_{st}| \quad (6)$$

$$k_{si,45°}=\sin\varphi_{si,\,45°}*|\underline{d}_{si,\,45°}| \quad (7)$$

$$k_{si,90°}=\sin\varphi_{si,90°}*|\underline{d}_{si,90°}| \quad (8)$$

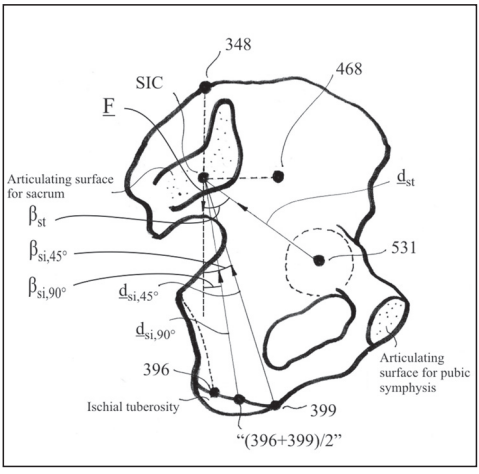

Figure 4. Anatomical points and vectors on the lateral view of the pelvis which have been used for calculating upper body weight moment. 531 is the center of hip joint; SIC is the sacroiliac joint center; 348 and 468 are two points which define SIC. The code numbers 348, 396, 399, 468, 531 are matched with anatomical points due to identification by Reynolds and colleagues[20]

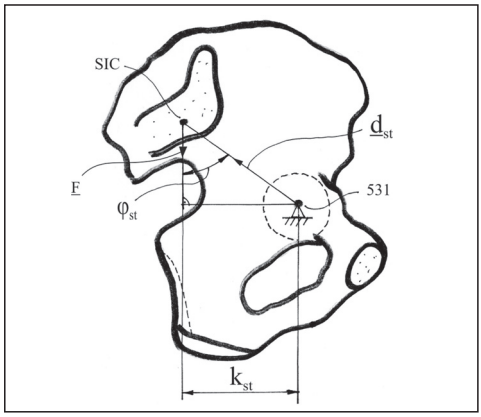

Figure 5. The lever arm of the upper body weight moment in standing posture

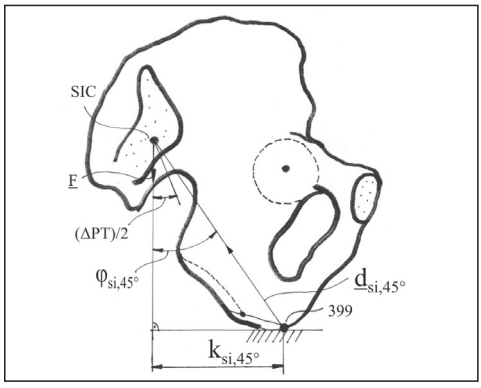

Figure 6. The lever arm of the moment in sitting with hip joint angle of 45°

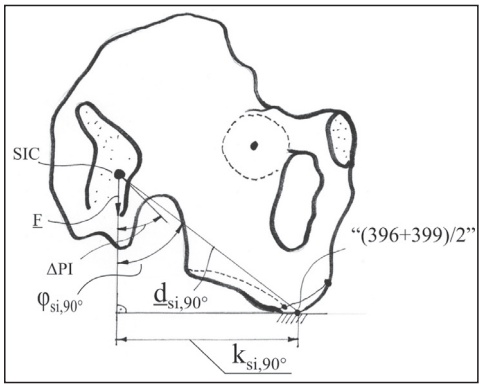

Figure 7. The lever arm of the moment in sitting with hip joint angle of 90°

where $\underline{d}_{st}$, $\underline{d}_{si,45°}$ and $\underline{d}_{si,90}$ are vectors which connect the acting line of the upper body weight and the rotation axis of the pelvis, and are transverse to each of those; and φ_{st}, $\varphi_{si,\ 45°}$ and $\varphi_{si,90°}$ are angles which are sum of PT and the smaller angle defined by vector $\underline{d}$ and upper body weight line. Results are shown in *Table 2*.

	body size/gender	model type	
		KD	EMGAO
M_{st} [Nm]	small female	9.8	10.7
	medium male	12.5	13.7
	large male	12.4	13.6
$M_{si,45°}$ [Nm]	small female	18.8	20.7
	medium male	23.3	25.7
	large male	24.3	26.9
$M_{si,90°}$ [Nm]	small female	29.5	32.8
	medium male	32.0	35.6
	large male	31.5	35.0

Table 2. Upper body weight moment acting on the pelvis (hip joint) in three different body postures

5. Conclusion

5.1. Estimating active muscle moment of the pelvis

Comparing the calculated results of passive and upper body weight moments of the pelvis it is found that the order of magnitude of passive moment is only comparable with the body weight moments in standing position. In both sitting posture with backward rotation of the pelvis there is an increase in body weights moment and a decrease in passive moment. Due to higher muscle activity exhausting of muscles and adaptation to a slumped position could be experienced after shorter period of sitting. Load on ligaments and discs and other muscles will be increased which can be harmful. In *Table 3* calculated moments and active muscle moments estimated as a difference between those moments are shown. The *Table 3* layout is simplified by averaging the upper body weight moment based on loading forces calculated with the two different models (KD, EMGAO) by Arjmand and colleagues.

On the basis of results of active muscle moment *(Table 3)* it is found that due to the lower muscle activity needed for it the 45° sitting posture can be maintained longer.

5.2. Limit of Study

Results have to be considered for a generic subject. Differences in moments of a specific subject could be due to the use of a generic function of passive elastic hip joint moment, a generic L5-S1 joint force, and generic lever arms of upper body weight. There is noticeable gap between measured and with model calculated data of passive elastic hip joint moment given by Riener and Edrich at the end of the range of motion of the joint.

	hip joint moment								
	Body weight moment [Nm]			Passive elastic moment [Nm]			Active muscle moment [Nm]		
	st	si,45°	si,90°	st	si,45°	si,90°	st	si,45°	si,90°
small female	10.2	19.7	31.2	8.6	2.7	0.3	1.6	17.0	30.9
medium male	13.1	24.5	33.8				4.5	21.7	33.5
large male	13.0	25.6	33.3				4.4	22.8	33.0

Table 3. Passive elastic moment; upper body weight moment; and active muscle moment estimated as a different of these two moments

REFERENCES

1. *Franco G, Franco F.* Voices from the past-De Morbis Artificum Diatriba (Diseases of Workers). American Journal of Public Health 2001; 91(9):1380-2.

2. Lumbágó. [cited 2014 Jan 05]. Available from: URL: *www.wikipedia.hu/lumbago.*

3. *Lloyd M, Gauld S, Soutar C.* Epidemiologic study of back pain in miners and office workers. Spine 1986;11:136–40.

4. *Ewans W, Jobe W, Scibert C.* A cross-sectional prevalence study of lumbar disc degeneration in a working population. Spine 1999;14:60–4.

5. *Videman T, Nurminen M, Troup JDG.* Lumbar spinal pathology in cadaveric material in relation to history of back pain, occupation, and physical loading. Spine 1990;15:728–40.

6. *Bakker E, Verhagen A, van Trijffel E, Lucas C, Koes B.* Spinal mechanical load as a risk factor for low back pain: a systematic review of prospective cohort studies. Spine 2009;34:E281–93.

7. *Roffey D, Wai E, Bishop P, Kwon B, Dagenais S.* Causal assessment of occupational sitting and low back pain: results of a systematic review." The Spine Journal 2010;10:252–61.

8. *Lis A., Black K, Korn H, Nordin M.* Association between sitting and occupational LBP. European Spine Journal 2007;16:283–98.

9. *Spyropoulos P, Papathanasiou G, Georgoudis G, Chronopoulos E, Koutis H, Koumoutsou F.* Prevalence of low back pain in greek public office workers. Pain Physician 2007;10:651-9.

10. *Janwantanakul P, Pensri P, Moolkay P, Jiamjarasrangsi W.* Development of a risk score for low back pain in office workers- a cross-sectional study. BMC Musculoskeletal Disorders 2011; 12:23.

11. *Rezaee M, Ghasemi M, Jafari NJ, Izadi M.* Low back pain and related factors among iranian office workers. International Journal of Occupational Hygiene 2011;3:23-8.

12. *Griffiths KL, Mackey MG, Adamson BJ, Pepper KL.* Prevalence and risk factors for musculoskeletal symptoms with computer based work across occupations. Work 2012;42:533-41.

13. *Stumpf B, Walker BM.* The Benefits of Pelvic Stabilization. Zeeland (Michigan): 2003. Sponsored by Herman Miller, Inc.

14. *Keegan JJ.* Alterations of the lumbar curve related to posture and seating, J Bone and Joint Surg (B) 1953;35:589–603.

15. *Harrison DD, Harrison SO, Arthur CC, Harrison DE, Troyanovich SJ.* Sitting Biomechanics Part I: Review of the Literature. Journal of Manipulative and Physiological Therapeutics 2000;23:37-47.

16. *Johns RJ, Wright V.* Relative importance of various tissues in joint stiffness. Journal of Applied Physiology 1962;17:824-8.

17. *Riener R, Edrich T.* Identification of passive elastic joint moments in the lower extremities. Journal of Biomechanics 1999;32:539-44.

18. *Arjmand N, Gagnon D, Plamondon A, Shirazi-Adl A, Larivičre C.* Comparison of trunk muscle forces and spinal loads estimated by two biomechanical models. Clinical Biomechanics 2009; 24:533–41.

19. *Endo K. Suzuki H, Nishimura H, Tanaka H, Shishido T, Yamamoto K.* Sagittal lumbar and pelvic alignment in the standing and sitting positions. J Orthop Sci 2012;17:682–686.

20. *Reynolds HM, Snow CC, Young JW*. Spatial Geometry of the Human Pelvis. Washington DC: Federal Aviation Administration (US), Human Aeromedical Office; 1982 March. Report No.: FAA-A2-82-9. Sponsored by Washington DC: Federal Aviaton Administration (US), Office of Aviation Medicine; Washington DC: National Highway Traffic Safety Administration.

Authors would like to thank the professional advices to Rita Kiss, director of the BME Biomechanical Cooperative Research Center.

Bálint Héra
Danubia Szabadalmi és Jogi Iroda Kft.
H–1368 Budapest, Pf. 198
Tel.: (+36) 1 411-8847

Dynamic time warping analysis in post-stroke rehabilitation

Bálint Magyar[1], Gábor Stépán[1], I-Ming Chen[2]
[1]Budapest University of Technology and Economics, Faculty of Mechanical Engineering, Department of Applied Mechanics
[2]Nanyang Technical University, School of Mechanical and Aerospace Engineering
magyar@mm.bme.hu

Abstract
This paper presents the application of the Dynamic Time Warping (DTW) algorithm in the analysis of human functional movements in activities of daily living (ADLs). Dynamic Time Warping was originally developed for automatic speech recognition, though the method has been adopted by several fields of biomechanics. As a part of the post-stroke rehabilitation project COSMOSYS, the aim is to quantify the ADL performances of hemiparetic subjects, hence to be able to track their progress during physiotherapy.

Keywords: dynamic time warping, stroke rehabilitation

Introduction

Dynamic Time Warping in automatic speech recognition is used to measure the similarity of two audio sequences, which may vary in time and speed. The sequences are warped non-linearly in the time dimension to determine the „score" of their similarity independent of certain non-linear variations in pace. The sequences are warped non-lin-early in the time dimension to determine the "score" of their similarity independent of cer-tain non-linear variations in pace for various applications of DTW.[1–6] The rehabilitation of hemiparesis after stroke demanded a comparison method that is able to express the correlation of two data sets. The aim is to evaluate the measured human functional movements also called Activities of Daily Living (ADLs), i.e. to qualify those with a single scalar. The difference of the measured and the reference ADL data sets can be used to evaluate the patients' performance.

The present approach bridges the gap between the objective sensory information available on normal and pathological human movements on one side and the subjective qualitative evaluation of these motions by the skilled professional in the form of performance scales on the other side. While the latter have already been standardized among clinical professionals, the error of human motion cognition by objective evaluation is still remarkable: evaluation of human movements may differ due to the imperfection of human cognitive capabilities, or simply from training, practice, institution, location and nationality of the clinical professional. The error can be radically reduced by the proposed co-iterative analytical-statistical method. Feeding of the DTW metrics into the robot controller makes the robot driven physiotherapy biomedically determined. In present approach the DTW metrics have been produced from measurements by 3D motion analyser whereas the robot can measure the same parameters from their integrated sensors: the motor encoders.

ADL Measurements

The ADLs to be measured on both healthy and post-stroke patients were selected by therapists of the Hungarian National Institute for Medical Rehabilitation, and the Singaporean Tan Tock Seng Hospital.
These ADLs are the following:
– picking up a phone from the table and placing it back;
– picking up a mug by its handle, moving it to the mouth and placing it back onto the table;
– opening and closing a window by its handle;
– picking up a towel, moving it to the face and placing it back;
– doing and undoing a zipper on a vest.

Measurement Device

The motion capture device, shown in *Figure 1,* consists of the Smartsuit and the Smartglove, developed in Nanyang Technological University, Singapore. Smartsuit is an IMU (Inertial Measurement Unit) based motion analyser for measuring upper arm and lower arm orientations. Smartglove acquires finger flexion-extension and palm orientation, by using optical encoders and an IMU. Finger flexion-extension data were excluded in the data mining analysis.

The pose of the hand is described by the feature vector $\mathbf{f}$, that is

$$\mathbf{f} = \left(\alpha_s, \beta_s, \gamma_s, \beta_e, \alpha_w, \beta_w, \gamma_w\right)^T \quad (1)$$

which contains the anatomic angles of the ***s***houlder, ***e***lbow and the ***w***rist. The definitions of these anatomic angles were inherited from the "Jack" human simulation software by Siemens PLM. The three IMUs in the Smartsuit and Smartglove provide the spatial orientations (roll, pitch, yaw) directly for the upper arm, lower arm and palm, while anatomic angles can be calculated afterwards. *Figure 2* illustrates the coordinate system and the reference points (S, E and W) on the arm. For a given length of the upper arm (L_{UA}), lower arm (L_{LA}) and palm (L_p), the coordinates of the reference points can be calculated as follows:

$$\mathbf{r}_{SE} = \mathbf{T}_y^{-\beta_s}\mathbf{T}_x^{\alpha_s}\mathbf{T}_z^{-\gamma_s}\mathbf{r}_{SE}^0, \quad (2)$$

$$\mathbf{r}_{SW} = \mathbf{T}_y^{-\beta_s}\mathbf{T}_x^{\alpha_s}\mathbf{T}_z^{-\gamma_s}\left(\mathbf{T}_y^{-\beta_e}\mathbf{r}_{EW}^0 + \mathbf{r}_{SE}^0\right), \quad (3)$$

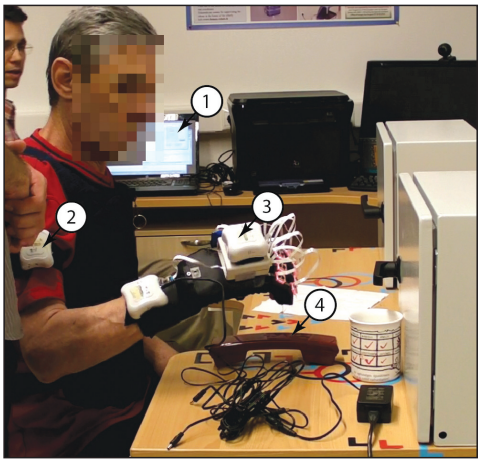

Figure 1. ADL measurement
1: data acquisition software; 2: Smartsuit;
3: Smartglove; 4: ADL items

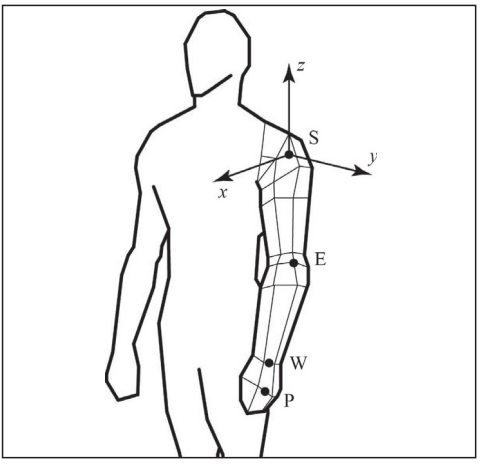

Figure 2. Base coordinate system
and reference points on the human arm

$$\mathbf{r}_{\mathrm{SP}} = \mathbf{T}_{\mathrm{y}}^{-\beta_{\mathrm{s}}} \mathbf{T}_{\mathrm{x}}^{\alpha_{\mathrm{s}}} \mathbf{T}_{\mathrm{z}}^{-\gamma_{\mathrm{s}}} \left(\mathbf{T}_{\mathrm{y}}^{-\beta_{\mathrm{e}}} \left(\mathbf{T}_{\mathrm{z}}^{-\beta_{\mathrm{w}}} \mathbf{T}_{\mathrm{x}}^{\alpha_{\mathrm{w}}} \mathbf{T}_{\mathrm{y}}^{-\gamma_{\mathrm{w}}} \mathbf{r}_{\mathrm{WP}}^{0} + \right. \right.$$

$$\left. \left. + \mathbf{r}_{\mathrm{EW}}^{0} \right) + \mathbf{r}_{\mathrm{SE}}^{0} \right) \tag{4}$$

where $\mathbf{r}_{\mathrm{SE}}^{0} = (0,0,-L_{\mathrm{UA}})^{\mathrm{T}}$, $\mathbf{r}_{\mathrm{EW}}^{0} = (0,0,-L_{\mathrm{LA}})^{\mathrm{T}}$, $\mathbf{r}_{\mathrm{WP}}^{0} = (0,0,-L_{\mathrm{P}})^{\mathrm{T}}$, with superscript 0 referring to the initial state, and $\mathbf{T}_{\mathrm{x}}^{\alpha}$, $\mathbf{T}_{\mathrm{y}}^{\beta}$, $\mathbf{T}_{\mathrm{z}}^{\gamma}$ are the rotation matrices with superscripts referring to the angle of rotation about the corresponding axes noted in the subscripts.

Dynamic Time Warping

A wide-spread method for computing the similarity between two time series is the Dynamic Time Warping algorithm, which is based on the alignment of significant patterns by locally deforming the time axis (hence the name warping) in order to minimize the cumulative difference between the aligned points. In order to obtain the optimal alignment, local compressions and shifts are achieved, thus, the method is suitable for matching time series containing patterns that are qualitatively similar but have different lengths and paces.[1]

Definitions

The inputs of the DTW algorithm are two data sequences, not necessarily containing the same number of samples. Let these sequences be noted by $\mathbf{F}^{\mathrm{I}} = (\mathbf{f}_1^{\mathrm{I}},...,\mathbf{f}_i^{\mathrm{I}},...,\mathbf{f}_n^{\mathrm{I}})$ and $\mathbf{F}^{\mathrm{II}} = (\mathbf{f}_1^{\mathrm{II}},...,\mathbf{f}_j^{\mathrm{II}},...,\mathbf{f}_m^{\mathrm{II}})$, where $\mathbf{f}_i^{\mathrm{I}}$, $\mathbf{f}_j^{\mathrm{II}} \in \mathbb{R}^q$ for $i \in [1,n]$, $j \in [1,m]$ and q is the dimension of the feature space. The outputs are the warping curve $(\Phi^{\mathrm{I}}, \Phi^{\mathrm{II}})$ and the DTW distance δ, where $\Phi^{\mathrm{I}} = (\phi_1^{\mathrm{I}},\ldots, \phi_k^{\mathrm{I}},\ldots, \phi_K^{\mathrm{I}})$ and $\Phi^{\mathrm{II}} = (\phi_1^{\mathrm{II}},\ldots, \phi_k^{\mathrm{II}},\ldots, \phi_K^{\mathrm{II}})$. These vectors contain the sample indices of $\mathbf{F}^{\mathrm{I}}$ and $\mathbf{F}^{\mathrm{II}}$ that should be selected to obtain the optimal fit $(\Phi^{\mathrm{I}}, \Phi^{\mathrm{II}} \in \mathbb{Z}^{\mathrm{K}})$. In order to calculate the warping curve, the constrained minimization problem

$$\left(\Phi^{\mathrm{I}}, \Phi^{\mathrm{II}}\right) = \arg \min_{\Psi^{\mathrm{I}}, \Psi^{\mathrm{II}}} \sum_{k=1}^{K} \mathrm{D}\left(\mathbf{f}_{\phi_k^{\mathrm{I}}}^{\mathrm{I}}, \mathbf{f}_{\phi_k^{\mathrm{II}}}^{\mathrm{II}}\right) \tag{5}$$

should be solved where D is the scalar-valued penalizing function that represents the distance between two feature vectors as detailed in (1). Several different sets of constraints can be found in the literature[1] for the warping curve $(\Phi^{\mathrm{I}}, \Phi^{\mathrm{II}})$. In this study, the following set is applied:

– asymmetric start-point constraint: $\phi_1^{\mathrm{I}} = 1$ and/or $\phi_1^{\mathrm{II}} = 1$,
– end-point constraint: $\phi_K^{\mathrm{I}} = n$ and $\phi_K^{\mathrm{II}} = m$,
– monotonicity: $\phi_{k+1}^{\mathrm{I}} \geq \phi_k^{\mathrm{I}}$ and $\phi_{k+1}^{\mathrm{II}} \geq \phi_k^{\mathrm{II}}$.

Following the determination of Φ^{I}, Φ^{II}, the DTW distance δ is calculated as follows:

$$\delta = \sum_{k=1}^{K} \mathrm{D}\left(\mathbf{f}_{\phi_k^{\mathrm{I}}}^{\mathrm{I}}, \mathbf{f}_{\phi_k^{\mathrm{II}}}^{\mathrm{II}}\right). \tag{6}$$

Comparison of Arm Postures, Penalizing Function

The similarity of two samples (i.e. feature spaces) can be quantified by evaluating the penalizing function $\mathrm{D}(\mathbf{f}_i^{\mathrm{I}}, \mathbf{f}_j^{\mathrm{II}})$. As shown in (1), the feature vector of a sample contains the anatomic angles of the shoulder, elbow and wrist:

$$\mathbf{f}_i^{\mathrm{I}} = \left(\alpha_{\mathrm{s}_i}^{\mathrm{I}}, \beta_{\mathrm{s}_i}^{\mathrm{I}}, \gamma_{\mathrm{s}_i}^{\mathrm{I}}, \beta_{\mathrm{e}_i}^{\mathrm{I}}, \alpha_{\mathrm{w}_i}^{\mathrm{I}}, \beta_{\mathrm{w}_i}^{\mathrm{I}}, \gamma_{\mathrm{w}_i}^{\mathrm{I}}\right)^{\mathrm{T}} \tag{7}$$

$$\mathbf{f}_j^{\mathrm{II}} = \left(\alpha_{\mathrm{s}_j}^{\mathrm{II}}, \beta_{\mathrm{s}_j}^{\mathrm{II}}, \gamma_{\mathrm{s}_j}^{\mathrm{II}}, \beta_{\mathrm{e}_j}^{\mathrm{II}}, \alpha_{\mathrm{w}_j}^{\mathrm{II}}, \beta_{\mathrm{w}_j}^{\mathrm{II}}, \gamma_{\mathrm{w}_j}^{\mathrm{II}}\right)^{\mathrm{T}} \tag{8}$$

The penalizing function is defined by

$$\mathrm{D}\left(\mathbf{f}_i^{\mathrm{I}}, \mathbf{f}_j^{\mathrm{II}}\right) = \left|\mathbf{f}_i^{\mathrm{I}} - \mathbf{f}_j^{\mathrm{II}}\right| + P_{\mathrm{v}} \frac{1}{\tau} \left| \left(\mathbf{f}_{i+1}^{\mathrm{I}} - \mathbf{f}_i^{\mathrm{I}}\right) - \right.$$

$$\left. - \left(\mathbf{f}_{j+1}^{\mathrm{II}} - \mathbf{f}_j^{\mathrm{II}}\right) \right| \tag{9}$$

$$+ P_{\mathrm{h}} \left(1 - \frac{\mathbf{f}_i^{\mathrm{I}} \cdot \mathbf{f}_j^{\mathrm{II}}}{\left|\mathbf{f}_i^{\mathrm{I}}\right| \left|\mathbf{f}_j^{\mathrm{II}}\right|} \right)$$

where τ is the sampling time, while P_{v} and P_{h} are weight parameters of the penalizing function for velocity and angle differences, respectively. The last term for the angle difference

represents 1–cos∈, where ∈ is the angle between the two feature vectors, which calculated by their scalar product.

In most of the automatic speech recognition applications the penalizing function consists only of the angle term, since the amplitude, i.e. the volume of the speech is not considered to increase or decrease the difference between two input sequences. Contrarily, in our case the feature vectors are containing the anatomic angles and/or anatomic positions of the human arm, therefore the Euclidean distances cannot be neglected, moreover, jerky motion (opposite to smoothly performed ADLs) has to be penalized by means of the term for velocities.

Computing the optimal alignment

In the first step, the calculation of the optimal alignment begins with the comparison of each sample $\mathbf{f}_i^{\mathrm{I}}$ to all other samples $\mathbf{f}_j^{\mathrm{II}}$, and the results obtained by the evaluations of the penalizing function are stored in matrix M_{ij}= D ($\mathbf{f}_i^{\mathrm{I}}$, $\mathbf{f}_j^{\mathrm{II}}$). Due to the term of the velocity differences, the last samples in each data sets cannot be used in the first and third term of the penalizing function (9), $i \in [1, n-1]$, $j \in [1, m-1]$. Matrix **M** is illustrated in *Figure 3*, in case of the comparison of two healthy subjects performing the same ADL (measured data shown in *Figure 5,* left column).

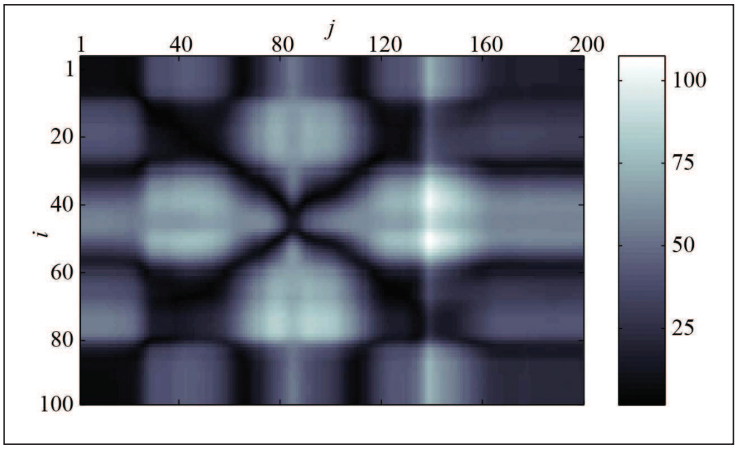

Figure 3.
Illustrating matrix **M**, for the comparison of data shown in *Figure 5,* see colorbar on the left for the values of each matrix element

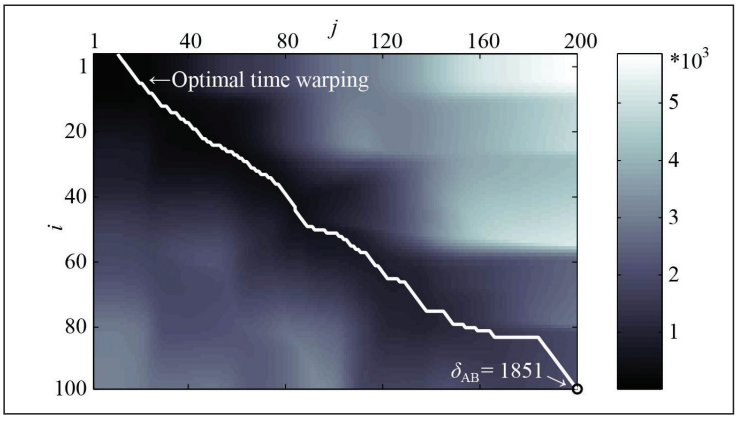

Figure 4.
Illustrating matrix **C** and the optimal time warping, in case of the comparison of data shown in *Figure 5,* see colorbar on the left for the values of each matrix element

Following the calculation of matrix **M**, the cumulated matrix **C** should be determined. Each element C_{ij} of matrix **C** represents the least possible sum of those elements of **M**, on which a step is taken when considering all the steps along the possible paths that connect elements M_{11} and M_{ij} fulfilling all the constraints listed in 3.1 including the monotonicity one (see *Figure 4*). The bottom right corner element of **C** defines the DTW distance δ.

Results

Comparison of ADL Performances

Figure 5 and *6* illustrate the results of two DTW analyses. In *Figure 5* the comparison of two healthy subjects (person *A* solid line and person *B* dashed line) is shown; both subjects are performing the same ADL, opening and closing a window. As it can be seen from the original measurement data (shown in the left column), there is a significant difference in the paces of the functional movements. Person *A* finishes in cca. 5 seconds, while person B needs cca. 10 seconds to complete the movement. The right column of the figure presents the aligned, that is the warped data in case of the optimal alignment (for penalizing parameters $P_v=25$ and $P_h=10$, the resulted DTW distance is $\delta_{AB}=1851$).

The comparison of a healthy (person *A*, solid line, same as in *Figure 5*) and a stroke affected (person *C,* dashed line) subject's ADL performances is shown in *Figure 6*. Though person *C* completes the function movement within roughly the time as person *B,* the DTW difference between *A* and *C* is significantly greater ($\delta_{AC}=3923$) than between *A* and *B*, hence this difference is induced by the variance in the measured anatomic angles (note that $\delta_{BC}=2661$).

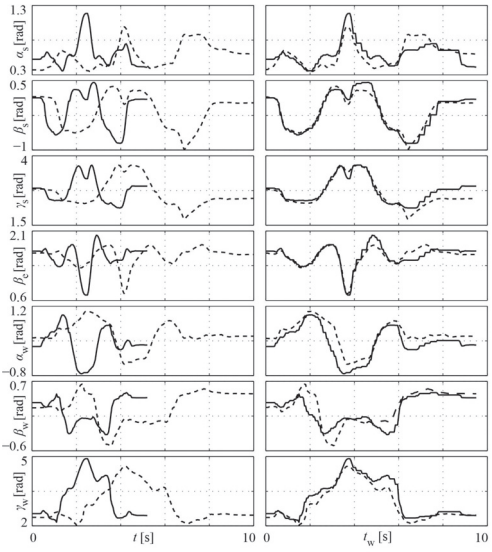

Figure 5. Comparison of two healthy ADL performances, person *A* solid line and person *B* dashed line, $\delta_{AB}=1851$

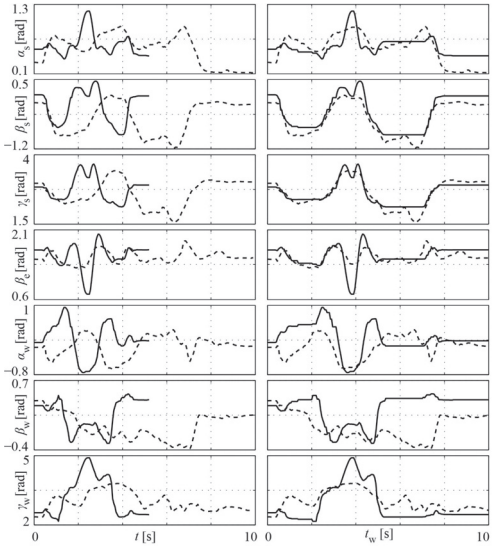

Figure 6. Comparison of a healthy and a stroke affected ADL performance, person *A* solid line and person *C* dashed line, $\delta_{AC}=3923$

Multidimensional Scaling Method

Following the determination of the DTW distances for all possible dataset-pairs, multidimensional scaling (MDS) is a commonly used method for visualizing the level of similarity of individual cases.[7] In this study, classical MDS method[8] is used. For a given distance matrix **D** that contains the pairwise differences of individual objects, MDS algorithm aims to place each object in an *N*-dimensional space such that the between-object distances are preserved as well as possible. Therefore, the difference matrix does not need to be an Euclidean distance matrix.

Scatter Plots of ADL Measurements

Since the DTW algorithm can produce such pairwise distances, that does not even obey the triangle inequality, MDS method is needed to optimize object locations for a two-dimension-

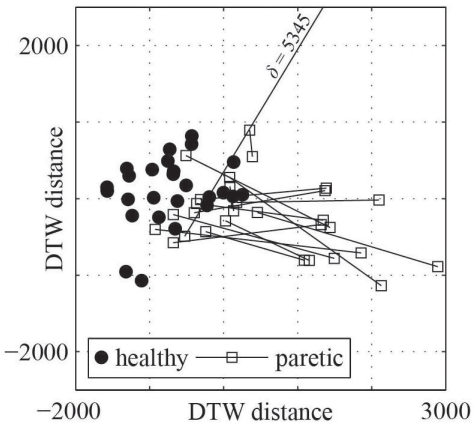

Figure 7. Scatter plot of ADL 1 performances (picking up a mug)

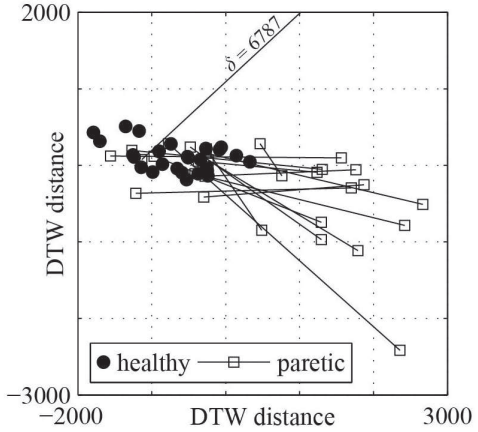

Figure 8. Scatter plot of ADL 2 performances (picking up a phone)

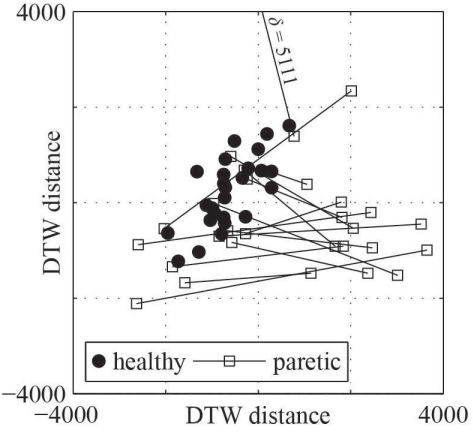

Figure 9. Scatter plot of ADL 3 performances (picking up a towel)

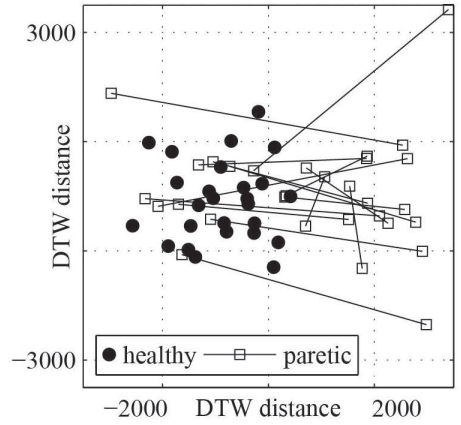

Figure 10. Scatter plot of ADL 4 performances (opening and closing a window)

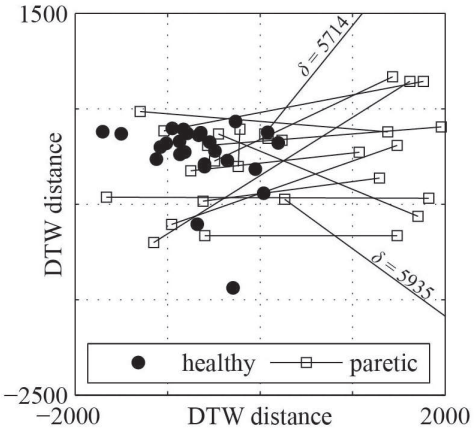

Figure 11. Scatter plot of ADL 5 performances (doing and undoing a zipper)

al scatter plot. These scatter plots are presented for all the 5 ADLs in *Figures 7–11*. In these figures solid discs represent healthy subjects, and squares represent the hemiparetic subjects, solid lines connect left and right hands of each stroke affected patient. By tuning P_v and P_h parameters in the penalizing function (9), two clusters had been evolved in the scatter plots. One contains the performances regarding both arms of healthy subjects and the non-paretic arm of hemiparetic subjects, and the other cluster is built up by the paretic arms of the stroke affected subjects.

Conclusions

According to the presented results, the performance of a post-stroke patient can be quantified as its distance from the cluster consisting of the reference ADL performances, i.e. the rehabilitation progress can be tracked by on objective, sensory based scale, lacking the possible errors due to human motion cognition. Due to the authors expectations, in the future standardized clinic scales, such as Fugl-Meyer, Asworth, Barthel, can be aided by DTW metrics. In order to achieve a good correlation with clinic scales, further evaluations are needed involving clinical professionals.

References

1. *Tormene P, Giorgino T, Quaglini S, Stefanelli M.* Matching incom plete time series with dynamic time warping: an algorithm and an application to p ost-stroke rehabilitation. Artifi cial Intelligence in Medicine 2009;45:11-34.

2. *Rath T, Manmatha R.* Word image matching using dynamic time warping. Manmatha R, editor. Proceedings of the IEEE computer society conference on computer vision and pattern recognition vol. 2; Los Alamitos, CA. USA: IEEE Computer So ciety; 2003. p. I I-521-7.

3. *Tuzcu V, Nas S.* Dynamic time warping as a novel to pattern recognition of ECG changes in heart rhythm disturbances. Jamsh idi M, Johnson M, Chen P, editors. Proceedings of the IEEE international conference on systems, man and cybernetics vol. 1; Los Alamitos, CA. USA: IEE E Computer Society; 2005. p. 182-6.

4. *Brina CD, Niels R, Overvelde A, Levi G, Hulstijn W.* Dynamic time warping: a new method in the study of poor handwriting. Human Movement Science 2008;27(2):242:55.

5. *Wu H, Kido R, Shioyama T.* Improvement of continuous dynamic programming for human gesture recognition. Proceedings of the 15th international conference on pattern recognition vol. 2; Los Alamitos, CA. USA: IEEE Computer So ciety; 2000. p. 945.

6. *Gollmer K, Posten C.* Supervision of bioprocesses using a dynamic time warping algorithm. Control Engineering Practice 1996;4(9):1287:95.

7. *Borg I, Groenen P.* Modern multidimensional scaling: theory and applications. 2nd ed. New York: Springer; 2005.

8. *Seber GA.* Multivariate observations. Hoboken, NJ: John Wiley and Sons, Inc., 1984.

This work was supported in part by the Agency for Science, Technology and Research, Singapore, under SERC Grant 092 149 0082 and the Media Development Authority, Singapore under NRF IDM004-005 Grants, project name COSMOSYS, and the Hungarian grant TÉT_08-SG-2010-0002.

Bálint Magyar
Budapest University of Technology and Economics, Faculty of Mechanical Engineering,
Department of Applied Mechanics
H–1111 Budapest, Műegyetem rkp. 5.
Tel.: (+36) 1 463-1436

Foreword

Borbás, Lajos – Kiss, Rita M.
president director
borbas@kge.bme.hu kissrit@t-online.hu

The Biomechanical Cooperation Research Centre of the Budapest University of Technology and Economics was founded by Professor Imre Bojtár in 2002 in order to coordinate biomechanical research at the University. The Biomechanical Cooperation Research Centre is an independent association of three departments of the Faculty of Civil Engineering, seven departments of the Faculty of Mechanical Engineering, one department of the Faculty of Chemical Technology and Biotechnology, and two departments of the Faculty of Transportation Engineering and Vehicle Engineering. The fundamental duty of the Biomechanical Cooperation Research Centre is to concentrate and coordinate and increase the efficiency of the work of the departments, professors and researchers taking part in the cooperation, as well as to develop and renew the pool of assets, to promote successful participation in domestic and international tenders, to keep organized contacts with medical universities, clinics and hospitals in Hungary, and to coordinate joint research projects. The Biomechanical Cooperation Research Centre plays an active role in the foundation of the Society of Biomechanics, its current operation, and in organizing Conferences of Biomechanics.

Members of the departments pertaining to the Biomechanical Cooperation Research Centre are devoted to support doctors' work and to educate replacement. Our research does not only involve a mechanical approach but includes all attempts, procedures and ways of thinking to assist those potentially in need to make their life easier and to give hope for the future solution of medico-biological problems seeming to be unsolvable today.

Research results of the departments pertaining to the Research Centre are published in Hungarian and international scientific reviews and conference publications. Nevertheless, this is the first occasion when the most important research findings of the Centre are published in the same volume.

When compiling this volume, our intention was to present the results of the most important topics of the Research Centre as a joint achievement of experienced head researchers and PhD students working together with them. We do hope that this volume of the Biomechanical Cooperation Research Centre provides a good kaleidoscope, not only to show the versatility of certain fields of science, but also the ability of the Research Centre to adapt to changing demands, standardized but versatile at the same time.

Dear Readers,

We do hope that you will find out about those scientific results in this volume that you can use in your subsequent research work. We hope to be able to soon cooperate with you in various research projects. Have a good time reading this publication!